GENERATION AND ANALYSIS OF STREAMWISE VORTICES FROM VORTEX TUBE APPARATUS

A Thesis
Submitted to the Graduate Faculty
of the
North Dakota State University
of Agriculture and Applied Science

By

Bailey McKay Carlson

In Partial Fulfillment of the Requirements
for the Degree of
MASTER OF SCIENCE

Major Department:
Mechanical Engineering

April 2020

Fargo, North Dakota

North Dakota State University
Graduate School

Title

GENERATION AND ANALYSIS OF STREAMWISE VORTICES FROM VORTEX TUBE APPARATUS

By

Bailey McKay Carlson

The Supervisory Committee certifies that this ***disquisition*** complies with North Dakota State University's regulations and meets the accepted standards for the degree of

MASTER OF SCIENCE

SUPERVISORY COMMITTEE:

Dr. Jordi Estevadeordal
Chair

Dr. Bora Suzen

Dr. Jacob Glower

Approved:

04/22/2020
Date

Dr. Alan Kallmeyer
Department Chair

ABSTRACT

A pressurized vortex tube is used to generate streamwise vortices in a wind tunnel and the resulting flow behavior is analyzed. The apparatus is intended to verify computational data from the AFRL by offering a method of conducting real-world counterpart experiments. The apparatus design process and other considered approaches are discussed. The vortex tube is operated at pressures of 20, 30 and 40 psi while the wind tunnel is operated at 3, 5, 10 and 20% capacity. Flow measurements are performed using particle image velocimetry to observe vortices and freestream interactions from which velocity and vorticity data is comparatively analyzed. Results indicate that vortex velocity greater than freestream flow velocity is a primary factor in maintaining vortex structures further downstream, while increased supply pressure and reduced freestream velocity also reduce vortex dissipation rate. A brief analysis of the vortex interaction with a downstream airfoil is presented to support future work.

ACKNOWLEDGEMENTS

This research was sponsored by the Air Force Research Laboratory at the Wright-Patterson Air Force Base, OH. They provided the simulation data used in this research and established the premise upon which this study was conducted, and I would like to thank them for this opportunity to perform research into such an interesting phenomenon.

Al Habib Ullah assisted me both in performing tests and in processing the collected data, for which I am very grateful. His insight and experience were most valuable throughout this research. Dr. Jordi Estevadeordal has been extremely helpful and supportive of me throughout my graduate studies and has made this experience much more enjoyable, and I would like to thank him for his continuing support. I would also like to thank Dr. Alan Kallmeyer for encouraging my interest in engineering over the 10 years I have been involved with activities and studies at NDSU, from BEST Robotics through the Mechanical Engineering graduate program.

DEDICATION

Dedicated to my parents, for giving me the best Part 1 of life I could ask for.

TABLE OF CONTENTS

LIST OF TABLES

LIST OF FIGURES

LIST OF ABBREVIATIONS

AFRL ..... Air Force Research Lab

NTSB ..... National Transportation Safety Board

FAA..... Federal Aviation Authority

PIV ..... Particle Image Velocimetry

CFD ..... Computational Fluid Dynamics

ABS ..... Acrylonitrile Butadiene Styrene

ID ..... Inner Diameter

DEHS ..... Di-Ethyl-Hexyl-Sebacat

CCD ..... Charge-Coupled Device

CNC ..... Computer Numerical Control

NASA ..... National Aeronautics and Space Administration

LIST OF SYMBOLS

α ..... Angle of Attack

AR..... Aspect Ratio

b ..... Wingspan

c ..... Chord Length

r_0 ..... Batchelor Vortex Radius

u_r ..... Batchelor Vortex Radial Velocity

u_θ ..... Batchelor Vortex Tangential Velocity

Γ_0 ..... Vortex Circulation

Δu ..... Batchelor Vortex Core Axial Velocity Deficit

q ..... Swirl Parameter

U_∞ ..... Freestream Velocity

V_0 ..... Maximum Circumferential Vortex Velocity

σ^2 ..... Vortex Stability Criterion

Re ..... Reynolds Number

Re_{c,U_∞} ..... Freestream Reynolds Number for Chord Length

M_∞ ..... Freestream Mach Number

ω_x ..... Axial Angular Velocity

ξ_x ..... Axial Vorticity

μs ..... Microseconds

dt ..... Differential Time

Q ..... Q-Criterion

Ω ..... Vorticity Magnitude

S ..... Strain Rate Magnitude

LIST OF APPENDIX FIGURES

CHAPTER 1: INTRODUCTION

Purpose

Formation flight is a commonly used technique in groups of aircraft to improve fuel efficiency. In order to improve upon the benefits obtained through formation flight, an understanding of the underlying physical phenomena is necessary. The primary factor in effective formation flight is the alignment of aircraft wings such that the wingtip vortices produced by a leading aircraft will intersect with the wing of a trailing aircraft in a way that increases lift and reduces drag. This intersection has been modeled numerically to produce valuable information about the nature of the fluid flow resulting from the interaction of the wingtip vortex with the trailing wing. In order to perform testing to verify such numerical methods, a robust real-world approach is needed to allow control over the flow parameters that are arbitrarily specified in simulations, and the device developed in this study is intended to provide this control. Therefore the goal of this research is to develop a method of producing controllable streamwise vortices for use in experimental analysis of vortex interactions with airfoils.

Outline

This thesis presents the development process of a vortex generation device for use in wind tunnel testing of the flow behavior of wingtip vortex interactions. Background information is presented in Chapter 2, regarding the nature of wingtip vortices, common concerns in the flight industry regarding their influence on other aircraft, and potential benefits to be gained by the successful management of streamwise vortices. Chapter 3 presents existing computational work performed on vortex interactions by the Air Force Research Lab (AFRL). This research provides the premise for the development of the vortex generator described in this thesis and

gives a reference for test data. The method of operation and development of this device are discussed in Chapter 4, and the apparatus and methodology used in testing is also described. Test results are presented in Chapter 5, including velocity and vorticity data in 2 and 3 dimensions, and a discussion of brief airfoil interaction testing. Chapter 6 concludes the thesis and summarizes the development and testing process of the vortex generator and discusses future work that may be done to further this research.

CHAPTER 2: BACKGROUND

Streamwise vortices are produced during the general operation of finite airfoil wings. The 3-dimensional nature of aircraft wings results in increased complexity of the surrounding airflow compared to that of a theoretical 2-dimensional airfoil. The high-pressure region created underneath the wing is responsible for producing lift; however, near the wingtips this pressure causes the air to be forced upwards and over the wing. The motion of this air produces a circulatory flow pattern that trails after the wing, known as a wingtip vortex. [1] The air that has circulated to the top of the wing now affects the wing's upper surface, producing a downward force in a process known as downwash, which reduces the effective angle of attack of the wing. [2] Conversely, the circulating air can also produce an upwards force, known as upwash, before it reaches the upper surface of the wing; however, since the axis about which the air is circulating is aligned with the wingtip, this upwash generally does not affect the wing generating the vortex. [3] The distribution of forces due to vortices is shown in Figure 1. To reduce the effects of downwash and increase flight efficiency, some aircraft utilize wingtip devices to alter the behavior of the circulating air. [3] While theorized prior to its first application, this approach was first implemented by Whitcomb in 1976 by adding nearly vertical wing-like plates known as winglets to the wingtips of aircraft. [4] The addition of wingtip devices increases the weight of the aircraft and causes increased drag due to the increase in surface area, but the benefits of increased fuel efficiency and maximum range often justify the decision. Wingtip devices may also be used to reduce takeoff noise and increase cruise altitude and speed. [3]

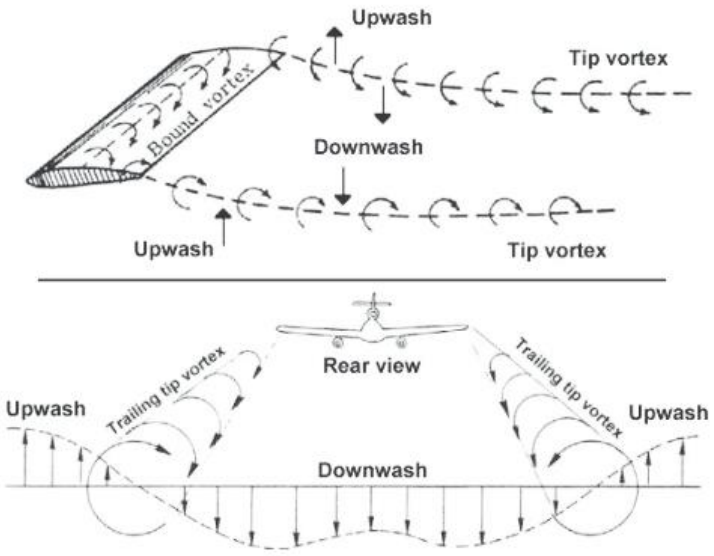

Figure 1: Downwash and Upwash Generation from Wingtip Vortices [5]

Wingtip vortices produced by finite airfoil wings can impact the flight characteristics of other aircraft. The vortices produced from the wingtip expand in diameter as they trail behind an aircraft. [3] Also known as wake turbulence, these vortices are produced during flight as well as during take-off and landing and have the potential to interfere with the operation of other aircraft with which they come into contact. An aircraft entering wake turbulence may experience sharp sudden aerodynamic moments that can be difficult to recover from. The National Transportation Safety Board (NTSB) records that in the United States between 1983 and 1993, at least 51 incidents and accidents occurred that were most likely caused by the interaction of aircraft with wake turbulence, some of which resulted in the death or injury of aircraft occupants or damage or destruction of one of the aircraft involved. To avoid incidents such as these, the FAA mandates that aircraft remain at a great enough distance away from the wake of other aircraft according to their weight classification, as larger aircraft produce stronger wakes. [6]

In a more useful situation, aircraft and birds flying in formation can take advantage of wingtip vortices to increase the lift produced by their wings and improve their efficiency. The

technique of formation flight is demonstrated by many species of birds: by flying in a V-shaped pattern, the wingtip vortices produced by the leading bird produce upwash, the opposite effect of downwash, on the trailing birds' wings when they are located within the upward-moving portion of the wingtip vortex. This upward component of the circulating air creates additional lift and thereby increases flight efficiency. A theoretical examination of this technique showed that the range of a flock of 25 birds would increase by 71% due to the benefits of upwash in formation flight. [7] Similarly for fixed-wing aircraft, the upwash of a leading aircraft may be used to provide additional lift for other aircraft, increasing efficiency and reducing fuel consumption. [8]

Streamwise vortices are also sometimes induced on the surface of an aircraft wing in order to delay boundary layer separation and improve fuel efficiency. These vortex generators are comprised of small fins mounted perpendicularly on the top surface of an aircraft's wings, at an angle to the incident airflow. As the vortices produced by the fins travel over the surface of the wing, they carry away some of the wing's slow-moving boundary layer and so delay the separation of the flow over the airfoil. [9] This interruption of flow separation is visible to some extent in the AFRL simulation data in Chapter 3.

CHAPTER 3: PRELIMINARY RESULTS

Overview

The interaction of a wingtip vortex with a trailing aircraft wing has been demonstrated and analyzed in a simulation performed at the Air Force Research Lab (AFRL) by Garmann and Visbal, in which the incident vortex from the leading wing causes attenuation and eventual dissipation of the wingtip vortex of the trailing wing. [10] This analysis provides the foundation for this study, in which a method of verifying the computational results in real-world testing is developed. The design process of a streamwise vortex generation device is discussed, followed by the testing regimen used to establish its robustness for future use. The device is operated under various configurations in multiple flow conditions, while particle image velocimetry (PIV) techniques are used to evaluate its capabilities. Data from real-world tests are compared with simulation results from the AFRL study in an effort to verify the accuracy of the simulation and prove the usefulness of the device.

Previous Research

The AFRL simulation demonstrates the transient behavior of an incident vortex interacting with an airfoil in the plane of the vortex, while the vortex is swept in the spanwise direction across the airfoil. When properly aligned, the opposing circulation of the incident vortex counteracts the circulatory flow of the wingtip vortex, diminishing the effects of both on the wing. Furthermore, as illustrated in Figure

2 below using Q-criterion isosurfaces of $Q = 5$, sweeping the incident vortex spanwise across the wing divides it between the two surfaces, but the two halves of the vortex partially reattach to the airfoil boundary layer after passing the leading edge. In the region of the wing that has been swept over by the incident vortex, a flow separation “bubble” is formed on both

surfaces of the wing, which prevents further wingtip vortices from reforming. This results in the elimination of downwash effects and thereby the effective lift of the trailing wing is increased. However, since this bubble is produced on both the high- and low-pressure surfaces, the flow separation reduces the effective aspect ratio of the wing, and induces a roll moment until the incident vortex has been swept far enough over the wing to balance the lift loss in the separation region with loading from the incident vortex. [10]

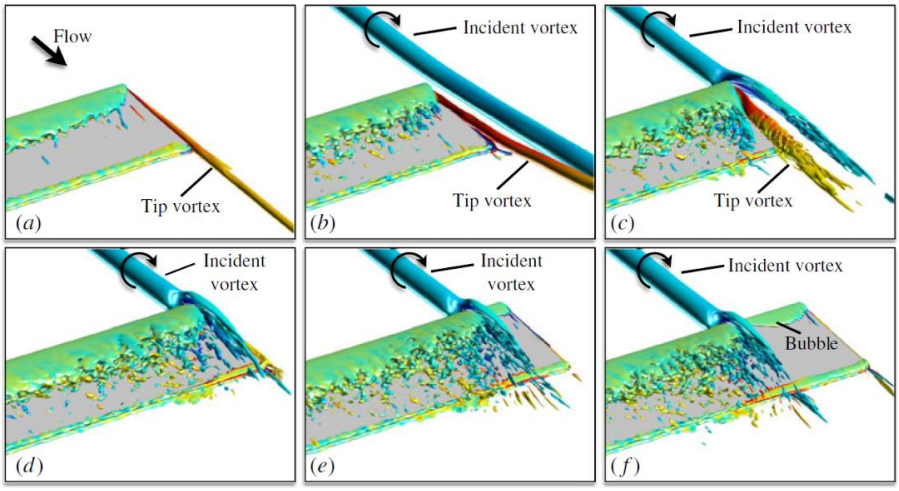

Figure 2: Attenuation of Wingtip Vortex by Incident Vortex [6]

The simulation was performed using a flat plate with angle of attack of $\alpha = 4°$ and an aspect ratio of $AR = \frac{b}{c} = 6$, where b is the wingspan and c is the chord length, to represent the wing of the trailing aircraft, and an analytically defined incident Batchelor vortex with radius $r_0 = 0.1c$, where c is the chord length of the "wing" being simulated. As presented in Garman and Visbal [10], this vortex is defined by the following equations:

$$u_r(r) = 0 \qquad \text{(Eq. 1)}$$

$$u_\theta(r) = \frac{\Gamma_0}{2\pi r}\left(1 - \mathrm{e}^{-(\mathrm{r}/\mathrm{r}_0)^2}\right) \qquad \text{(Eq. 2)}$$

$$u_x(r) = 1 - \Delta u \mathrm{e}^{-(\mathrm{r}/\mathrm{r}_0)^2} \qquad \text{(Eq. 3)}$$

In these equations, Γ_0 is the vortex circulation and Δu is the vortex core axial velocity deficit. This deficit is specified as $\Delta u = 0.4U_\infty$, where U_∞ is the freestream velocity, to produce a maximum circumferential velocity of $V_0 = 0.5U_\infty$. The swirl parameter q is used define the strength of the vortex, where q is defined by

$$q = \frac{\Gamma_0}{2\pi r_0 \Delta u} \approx 1.567 \frac{V_0}{\Delta u} \quad \text{(Eq. 4)}$$

This equation can be rewritten to express the circumferential velocity in terms of the swirl parameter as shown in (Eq. 5):

$$u_\theta(r) = \frac{q\Delta u}{r/r_0}\left(1 - \mathrm{e}^{-(r/r_0)^2}\right) \quad \text{(Eq. 5)}$$

This allows the use of (Eq. 6), an additional criterion defined by Leibovich and Stewartson [11], to be used to ensure the stability of the vortex:

$$\sigma^2(r) = \frac{2u_\theta(ru'_\theta - u_\theta)\left(u_\theta^2/r^2 - u'^2_\theta - u'^2_x\right)}{(ru'_\theta - u_\theta)^2 + (ru'_x)^2} < 0 \quad \text{(Eq. 6)}$$

By substituting the definitions of the velocity components in (Eq. 4) and (Eq. 5) into (Eq. 6), it can be determined that the minimum allowable value for q to maintain stability of the vortex is $q \geq \sqrt{2}$, and a value of $q = 2$ was used to define the incident vortex. The freestream flow was defined by $Re_{c,U_\infty} = 20000$ and $M_\infty = 0.1$ to improve performance of the FDL3DI numerical solver. [10] The swirl parameter can be related to axial vorticity by the following equation:

$$q \approx 1.567 \frac{V_0}{\Delta u} = \frac{1.567}{\Delta u}\left(\frac{\omega_x}{r_0}\right) = \frac{0.7935\xi_x}{r_0 \Delta u} \quad \text{(Eq. 7)}$$

Here ω_x is the angular velocity of the vortex at its outer radius about the axial direction x, and ξ_x is the axial vorticity and is defined by $\xi_x = 2\omega_x$.

Since these vortex characteristics are dependent on arbitrary values, the geometry of the simulated wing, and the freestream velocity, a real-world test would require a means of producing vortices that could be manipulated to match the conditions of the simulation, and the vortex generator developed in this study is intended to provide this control over the incident vortex.

Propeller Vortex Generator

The use of a propeller to generate streamwise vortices was considered early in the design stage of this study. ANSYS simulations of a propeller contained inside a cylindrical chamber showed that such a device would be capable of producing streamwise vortices. Figure 3 below shows the streamlines from a simulation of a propeller with diameter 1.25 inches and 45 degree blade pitch angle rotating at 60 rpm, with flow entering the inlet of the cylindrical chamber at 30 m/s. This series of simulations was performed using a k-ε model with 5% turbulence, with high resolution advection scheme and first order turbulence numerics, and a residual target of 1e-6. Although the simulations indicated that a propeller would be capable of and effective at generating streamwise vortices, the size of the propeller needed to produce a vortex at the scale of the AFRL simulation presented significant manufacturing problems, as detailed in Chapter 4, and further development on a propeller-based vortex generator was stopped to focus on other potential designs that could be manufactured at the desired scale.

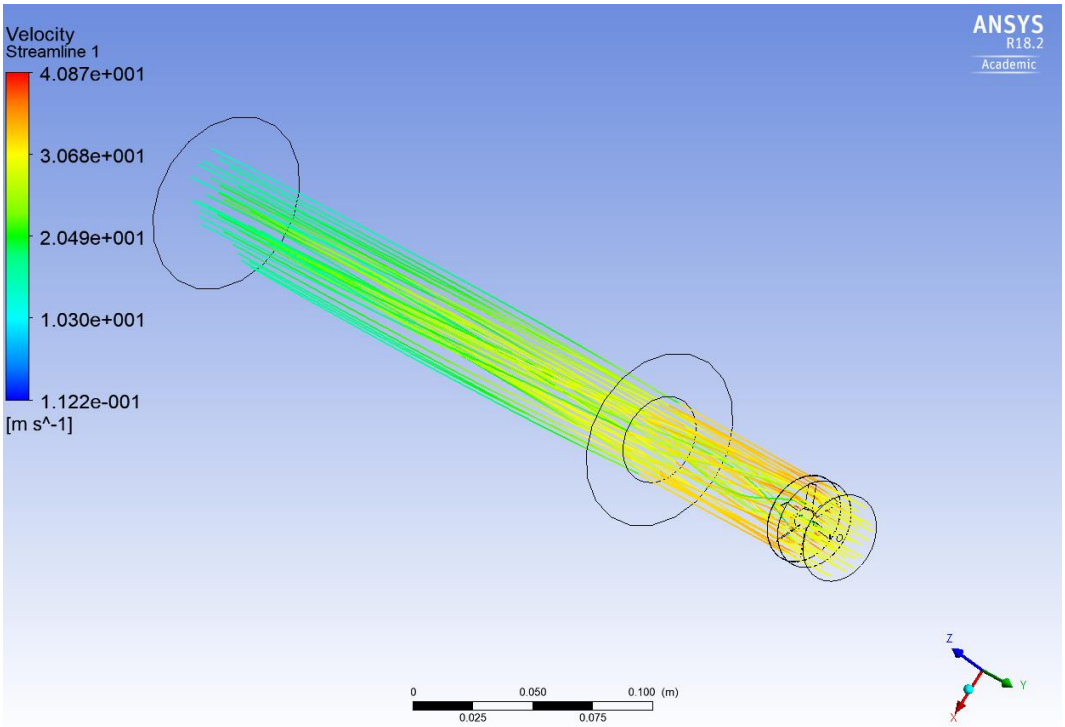

Figure 3: Proof-of-concept ANSYS Simulations of Propeller Vortex Generation Capability

Pressurized Vortex Tube

The generation of streamwise vortices using a pressurized vortex tube was simulated using ANSYS software to perform a computational fluid dynamics (CFD) analysis of the device to determine if it would be capable of producing vortices in the downstream flow. Figure 4 shows the streamlines produced by a proof-of-concept apparatus simulated with the CFX solver with an inlet pressure of 60 psi in a flow with a freestream velocity of 30 m/s, and with the same solver conditions as in the propeller simulations. Initially an attempt was made to increase the strength of the vortex by using a larger chamber to circulate the inlet flow before forcing it into the extended chamber, however the simulations indicated that this had the opposite effect and reduced the speed of the outlet flow. Based on these results the constant radius chamber design was selected for manufacturing.

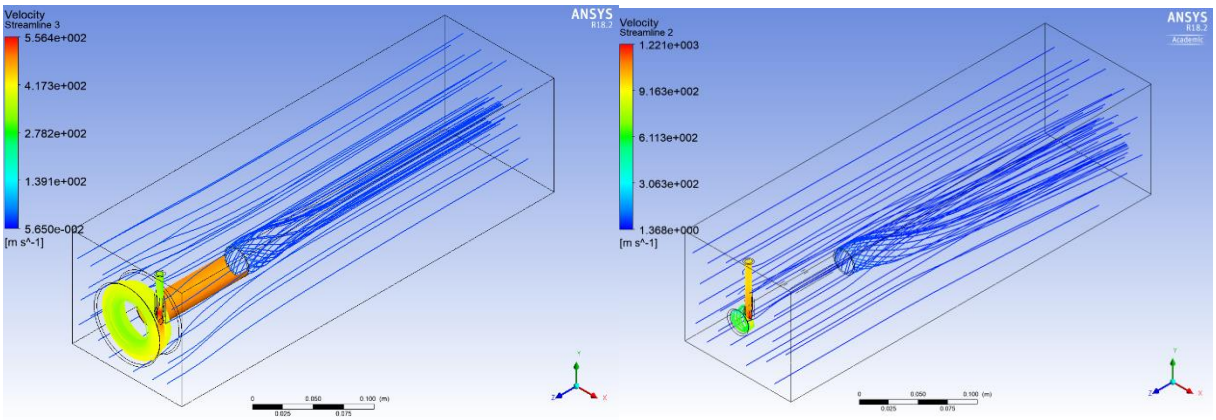

Figure 4: Proof-of-concept ANSYS Simulations of Pressurized Vortex Tube

Scope and Domain of Analysis

This study aims to perform qualitative analysis on the behavior of vortices produced by the vortex generator designed herein, and to facilitate the use of this device in verifying the previously discussed AFRL simulation. The pressurized vortex tube will be operated with several pressures of supplied compressed air, and at several wind tunnel speed settings. The available hardware is a limiting factor in the observation of the produced vortices, and the maximum speed of the data collection process was too much slower than the timescale of the vortex structures to collect time-resolved data due to the limitations of the laser apparatus. As such, only snapshots of the vortices could be collected, separated by the minimum allowable interval stipulated by the laser's capabilities.

The flow region immediately following the vortex generation device is a primary region of interest for this study, as the generated vortex structures will be at their highest strength and greatest integrity shortly after exiting the vortex tube. Also relevant is the behavior of the vortex structures after they have traveled downstream and their interactions with the freestream flow. This behavior is important since the presence of an obstruction in the flow, in this case the vortex generator, could potentially lead to vortex shedding, i.e. producing vortices in the plane of the

flow. Note that this is a different phenomenon than the intended goal of producing streamwise vortices, and the produced vortex sheets could cause unwanted additional flow behavior inconducive to the measurement of the streamwise vortices. In the case of the interaction of streamwise vortices with a downstream airfoil such as that presented in the AFRL simulation, accurate measurement during real-world testing may be made more difficult by the vortex sheets interacting with the airfoil in addition to the streamwise vortices. To avoid this added difficulty, the vortex generator would be placed upstream from the airfoil far enough to allow the vortex sheets to dissipate, but close enough that the streamwise vortex structures remain intact until reaching the airfoil. Thus, observation of the downstream vortex behavior is greatly beneficial to ensuring the vortex generator designed in this study is capable enough for use in future endeavors.

CHAPTER 4: EXPERIMENTAL SETUP

Overview

The goal of the vortex generator design process was to produce an apparatus that could be used to perform a real-world test to verify the accuracy of the aforementioned AFRL simulation. To do so, the design would need to allow control over the strength of the vortices produced to keep the structures intact further downstream and maintain their vorticity during their travel. Additionally, scalability was also required to produce vortices with a wide range of diameters in order to accommodate varying sizes of wings that might be used in testing. Initially 2-dimensional PIV was performed for preliminary analysis of the vortex flows, but the 3-dimensional nature of the AFRL simulation and the flow phenomena itself emphasized tomographic PIV as the most suitable approach to measurement for comparative analysis, and as such this technique was also employed in testing.

Pressurized Vortex Tube

The first method used for vortex generation was the pressurized vortex tube. This device circulates compressed air in a cylindrical chamber and then releases the air into the freestream flow. These devices are used in industry to produce separate streams of higher and lower temperature air from a single supply [12]. The device's operation is illustrated in Figure 5 below. Compressed air is introduced into the chamber from a tangential port near the front of the chamber's interior. The tangential airflow then circulates along the length of the device, and upon reaching the end of the chamber the central portion of the vortex air is reflected back through the chamber to exit the front of the device, while the heated outer air is released through a valve at the back end. In this study, the valve is removed entirely to allow the air to continue its circulatory pattern outside the device, forming a streamwise vortex. This approach allows for the

strength of the produced vortex to be manipulated by increasing or decreasing the pressure of the compressed air supplied to the vortex tube.

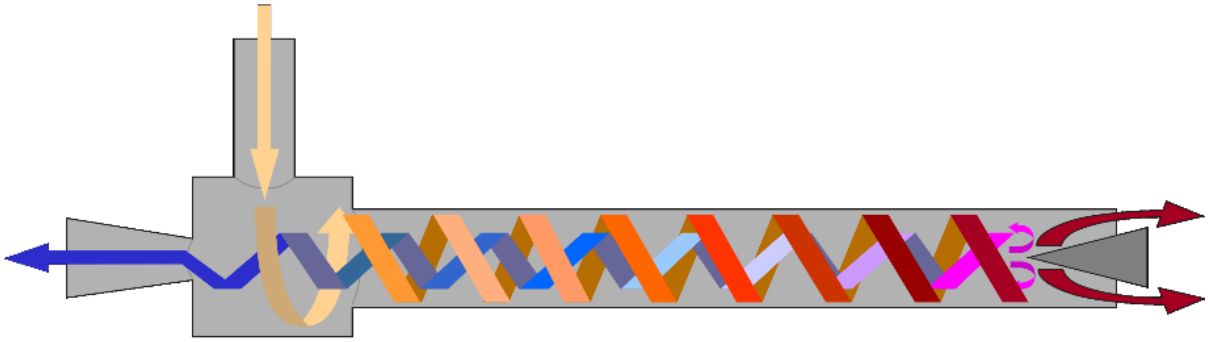

Figure 5: Vortex Tube Method of Operation (Public Domain Image)

The pressurized vortex tube was constructed by 3D printing with ABS plastic with a cylindrical chamber length of 6 inches, an internal diameter of 0.25 inches and an external diameter of 0.375 inches. The tangential inlet had an internal diameter of 0.0625 inches and was supplied with compressed air through 0.036 inch ID tubing. The dimensions of the device were chosen to conform to the vortex size relations imposed by the AFRL simulation: streamwise vortices with an outer diameter of 0.25 inches corresponds to an airfoil chord length of 1.25 inches, and for an aspect ratio of 6 this airfoil would have a wingspan of 7.5 inches. As a result the wingtip of the airfoil of corresponding size would be located near enough the center of the 12 in^2 wind tunnel test section, with the goal of sufficient spacing to avoid interacting with the boundary layers on the wind tunnel walls. Both ends of the chamber were left open in the initial design of the part to allow future testing to investigate the effects of allowing the freestream flow to enter the chamber, but the front end of the chamber was sealed during testing. To determine the effects of changes in air supply pressure on the produced vortices, the device was operated with supply pressures of 20, 30 and 40 psi. The device is pictured in Figure 6 below, mounted on a slider system to allow spanwise motion for transient tests.

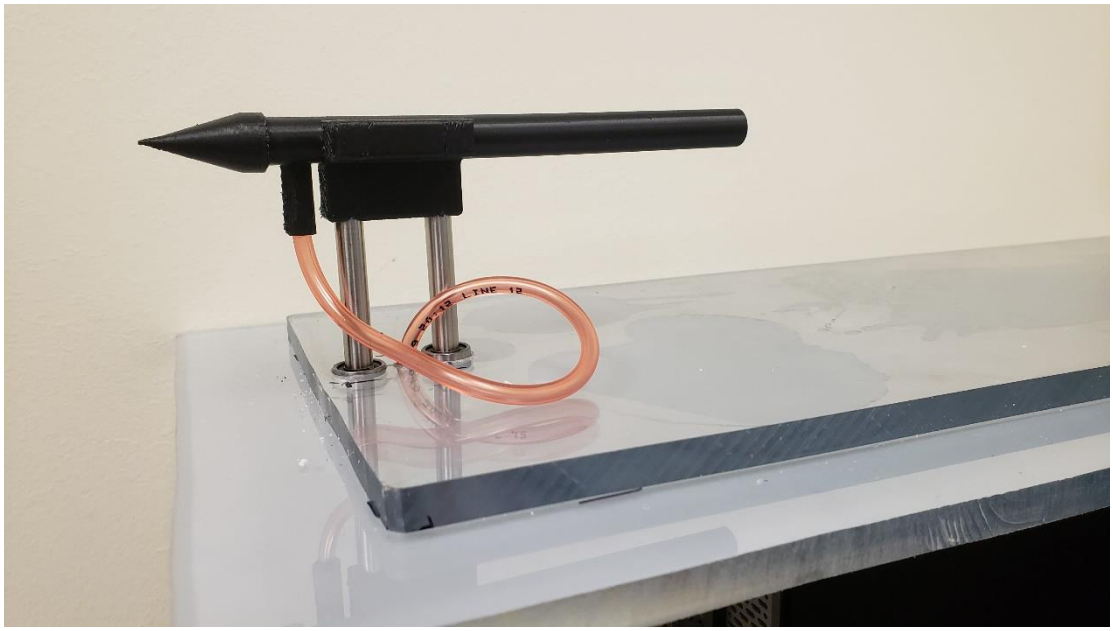

Figure 6: Pressurized Vortex Tube Outside Wind Tunnel

Wind Tunnel

Tests were conducted inside a FloTek 1440 wind tunnel with a test section area of 12 in^2 that was operated at various speeds for each vortex generation apparatus. For each configuration of each vortex generator, the wind tunnel was operated at speeds ranging from 3% to 43% for the 2-dimensional PIV tests, and from 3% to 20% for 3-dimensional tests. The corresponding freestream velocities were then determined for each wind tunnel percentage using separate Pitot tube measurements obtained prior to testing, with the results shown in Table 1. During previous tests in other research, the wind tunnel had displayed some irregularities in the test section flow profile, likely due to its square inlet. However, these irregularities were only observed very near to the test section walls and were avoided by placing the vortex generator in the center of the test section to ensure a uniform freestream flow was experienced during testing. As previously discussed, avoiding the effects of the irregularities was also a factor in selecting the dimensions of the vortex tube.

Table 1: Wind Tunnel Percentage Conversions

Wind Tunnel Percentage	**Freestream Velocity (m/s)**	**Reynolds Number**
3%	0.21	41.731
5%	2.9	576.28
10%	4.32	858.462
20%	8.58	1705
43%	18.25	3626.45

The freestream velocity was responsible for carrying the streamwise vortex away from the generator, and as such an increase in freestream velocity would affect the periodicity of the vortices. While even the Reynolds number of the 43% setting is much less than the value of $Re = 20000$ used in the AFRL simulation, during testing the vortex structures were significantly disrupted by flows at this and higher velocities, making measurement difficult to perform accurately. This was a contributing factor to the decision to cancel the 43% speed setting tests for both 2- and 3-dimensional PIV.

The slider on which the vortex tube was mounted was integrated into a removable panel that could be inserted into a wall of the wind tunnel test section. This customizable wall allows the tunnel to be reconfigured for different test setups, which was necessary for the airfoil interaction testing as discussed in this chapter and Chapter 5.

Particle Image Velocimetry

The vortices produced by the generation apparatus were observed using both 2D and Tomographic 3D PIV approaches. Small droplets of sub-micron diameter were introduced into the wind tunnel as an aerosol produced from atomization of DEHS oil. Pressurized air is injected into a tank of this oil, producing droplets around air bubbles. The oil-air mixture is then carried

to the diffusors where it is released as a mist into the inlet of the wind tunnel. Due to their small size, gravitational and interparticle forces are ignored, and these droplets are characterized as accurately following the flow path of the airflow inside the wind tunnel. The density of the mist released into the wind tunnel was controlled by modifying the pressure of the supplied air to ensure that the proper particle density was present during testing. Not enough particles in the flow would prevent accurate measurements from being obtained, while too many particles would lead to excessive computational effort being required to process the resulting images. The particle seeding apparatus is shown in Figure 7.

Figure 7: Wind Tunnel Particle Seeder Apparatus

The droplets were then illuminated by a dual-beam laser, shown in Figure 8 below. For 2D PIV, the laser was expanded into a vertical sheet parallel with the flow, which was centered at the axis of the vortex generator. For tomographic PIV, the laser was expanded to shine over a volumetric region of interest for the apparatus, specifically the flow region immediately following the outlet of the vortex tube. The dimensions of this region remained unchanged

between tests to allow comparison of the data between configurations without needing to account for differences in location of the test volume.

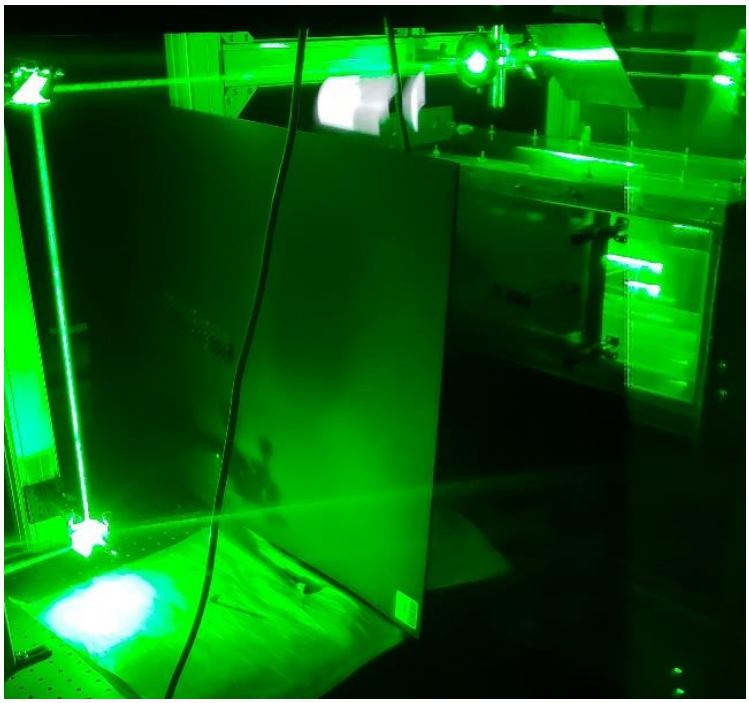

Figure 8: PIV Laser Apparatus

For each measurement instance, the laser emits two pulses separated by less than 100 μs to illuminate the region and capture two images of the particles. A timing interval for the pulses is selected that is short enough that the displacement of the particles is small enough for the correlation algorithm to identify the individual particles' positions in both frames, but also large enough that the difference of the particles' positions is great enough to measure. When chosen properly, the resulting vectors obtained from the measured displacement and time provide an effectively instantaneous velocity field of the observed flow region.

The selection of this interval is complicated by the presence of multiple flow regions with varying velocities; in such a flow, the proper interval may be suitable for a slower flow but unable to accurately measure the faster flow region, or vice versa. This problem limited the velocities that could be tested in the wind tunnel, as even at the 43% setting the difference

between the freestream velocity and vortex velocity made accurate measurement difficult, which also contributed to the decision not to use the 43% setting for data collection. The selected 2D timing intervals for each configuration are presented in Table 2, and the timing intervals for tomographic measurement are given in Table 3.

Table 2: Timing Intervals for 2D PIV

2D	**20 psi**	**30 psi**	**40 psi**
3%	40 μs	40 μs	40 μs
5%	40 μs	30 μs	30 μs
10%	30 μs	30 μs	30 μs
20%	30 μs	30 μs	30 μs

Table 3: Timing Intervals for Tomographic PIV

3D	**20 psi**	**30 psi**	**40 psi**
3%	60 μs	40 μs	40 μs
5%	70 μs	60 μs	50 μs
10%	70 μs	60 μs	50 μs
20%	60 μs	50 μs	60 μs

Images of the illuminated droplets were then captured using CCD PIV double-frame cameras with 1600x1200 resolution mounted outside the tunnel at various positions and angles. These cameras are designed to rapidly capture two images corresponding to the two laser pulses in each measurement instance. During 2D operation, the cameras captured images spanning approximately 40 mm (1.575 inches) in the *x*-direction and 30 mm (1.181 inches) in the *y*-direction, while the tomographic camera arrangement, shown in Figure 9, captured images in

their own local coordinate systems. For tomographic operation, the resulting images were used to reconstruct the 3-dimensional positions of the droplets within the flow region of interest in both frames. For both 2D and 3D approaches, a cross-correlation algorithm was applied to the two consecutive frames to identify the displacement of the particles between frames. As previously mentioned, these displacement vectors, when divided by the time interval between frames, produce effectively instantaneous 2D (u, v) or 3D (u, v, w) velocity fields of the flow for individual camera views or tomographic reconstructions, respectively.

Figure 9: Camera Apparatus for Tomographic PIV

Airfoil Interaction Test Apparatus

After testing of the pressurized vortex tube was complete and the device's effectiveness and capabilities had been demonstrated and quantified, an additional set of tests was performed to observe the interaction of the generated streamwise vortices with a downstream NACA 0012 airfoil in the manner of the AFRL simulation. While this series of tests was limited in scope, it was useful to determine the vortex generator's effectiveness for use in more varied future tests to perform a robust verification of the simulation results. The airfoil was positioned at a specific

angle of attack using an external motorized actuation system designed to allow rapid pitching motion, shown in Figure 10, and while this functionality was not utilized in these static tests, the apparatus allowed the angle of attack to be configured repeatably.

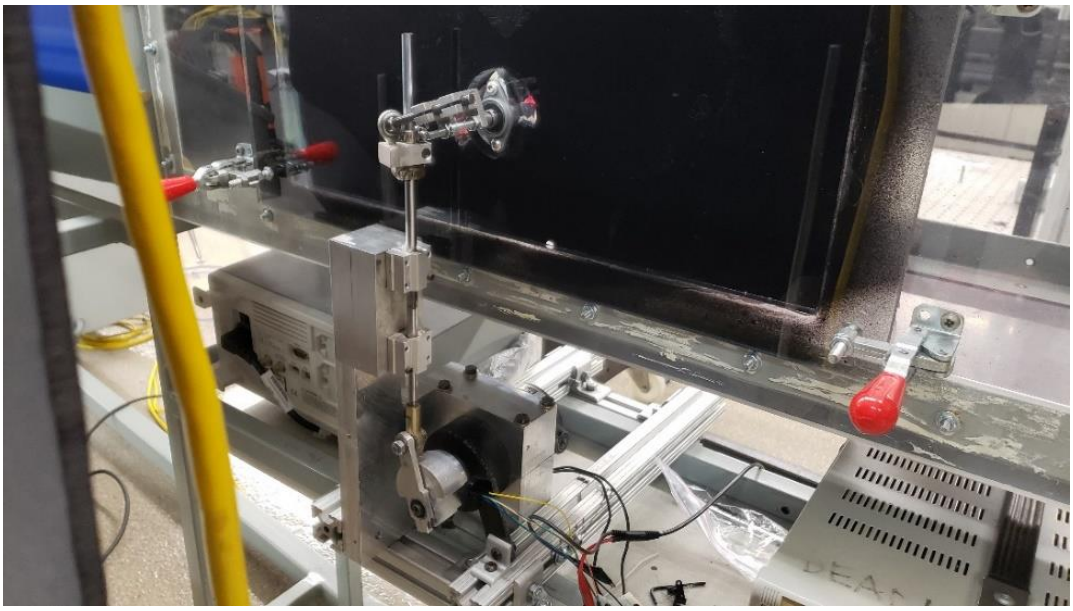

Figure 10: Airfoil Actuation Apparatus

In order to use this actuator, the removable section of the wind tunnel wall needed to be replaced with a dedicated panel made for use with this system. Thus the vortex generator was instead mounted from the bottom of the test section at the same vertical location, while being slightly offset inwards along the airfoil, as seen in Figure 11. An additional mounting bracket was included in the design of the vortex tube to allow an offset in the positioning of the device without requiring excessive additional geometry or parts that could lead to enhanced wake production. This offset was deliberately introduced to avoid projecting the laser volume over the wingtip, which, although ideal for testing wingtip vortex dissipation, would have produced significant glare from the laser in the camera views, introducing noise and preventing them from capturing accurate images.

Figure 11: Vortex Generator Setup for Airfoil Interaction

Additional Considered Designs

As previously alluded to in Chapter 3, another option that was considered for vortex generation was the use of a propeller mounted streamwise inside a tube to contain the circulatory flow produced by the motion of the blades further downstream. As shown in Figure 12 below, CFD simulations of parametric propellers in the previously used flow conditions indicated that the strength of the produced vortex was most influenced by the propeller's blade pitch angle, while rotational speed had only a minor effect.

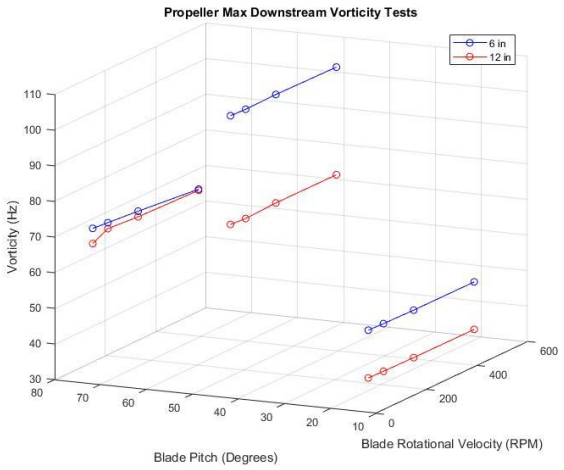

Figure 12: Propeller Blade Pitch and Vortex Strength Simulation Analysis

A variable blade pitch propeller was designed to allow the strength of the generated vortex to be controlled during testing and to reduce the setup time required for swapping out

propellers between tests. This apparatus would consist of a motor mounted outside the wind tunnel and a pulley system to drive the propeller inside the test section. Presented in Figure 13, the blade pitch would be controllable by means of a brake cable mounted coaxially to the propeller axle, which would actuate a piston that pressed down on small tabs on the blades' axles to rotate the blades about their centers of rotation, changing their pitch. Small springs located underneath each tab would return the blades to their initial angular position when the piston was retracted. This approach would allow the rotational positioning of the blades to be controlled with a linearly positioned actuator.

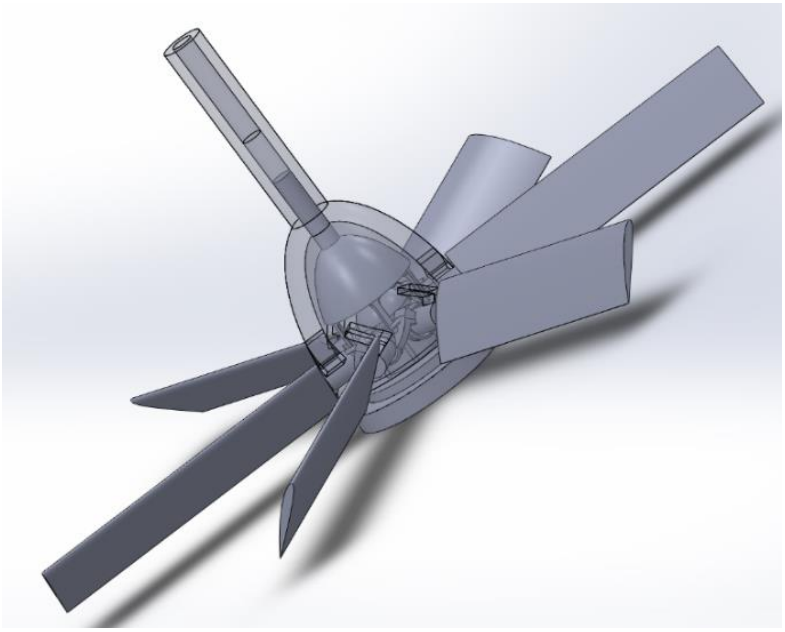

Figure 13: Variable Pitch Propeller CAD Design

However, the complexity of the blade pitching mechanism, illustrated in more detail in Figure 14, made manufacturing of the propeller impractical at the desired scale. While simulations showed that a propeller would likely have been effective for producing streamwise vortices, the scale required by the AFRL simulation introduced further difficulty. To produce a vortex of the prescribed radius of 0.1*c* for a wing with an aspect ratio of 6, either the wing would need to have an excessive chord length for the dimensions of the wind tunnel test section, or the

propeller would need to be small enough to produce a vortex with diameter of much less than 1 inch. Even with a wingspan of 12 inches, the maximum wingspan that could physically fit inside the wind tunnel test section, the required propeller diameter would be 0.4 inches, which was difficult to prototype with available 3D printing machinery before manufacturing with CNC operations. Therefore since testing of this device could not be readily performed in the timescale of this project, this approach was dropped in favor of the pressurized vortex tube.

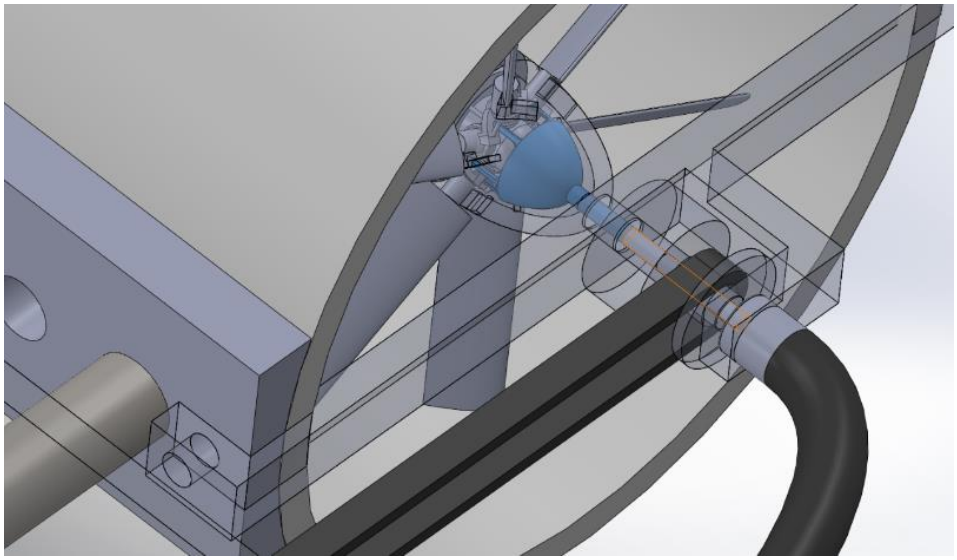

Figure 14: Variable Pitch Propeller Detail

The final considered vortex generation apparatus consisted of a vibration motor with eccentric mass axially aligned with the freestream flow. The motor casing was 6 mm (0.236 inches) in diameter and 12.21 mm (0.481 inches) in length, with the eccentric mass having a diameter of 5 mm (0.195 inches) and length of 4 mm (0.1575 inches). The periodic rotation of the mass mounted eccentrically on the motor shaft produced a streamwise vortex through disruption of the incident flow. The motor was planned to be operated at voltages between 1.5V and 3V, and by varying the voltage supplied to the motor the rotational velocities and thus the strength of the produced vortices could be controlled. However, upon testing this device as

shown in Figure 15, the produced vortices were too weak to accurately observe, and additional testing was discontinued.

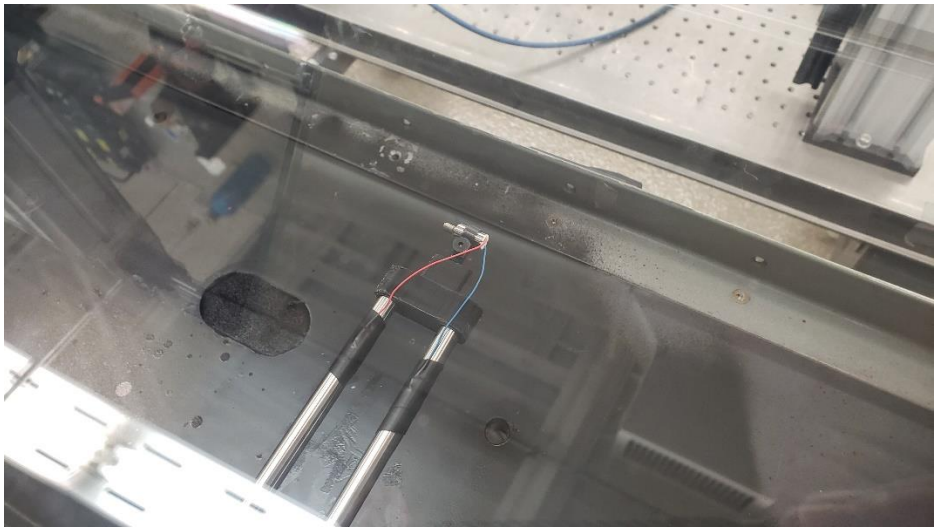

Figure 15: Vibration Motor in Wind Tunnel

CHAPTER 5: RESULTS AND DISCUSSION

2D Test Results Overview

The pressurized vortex tube was tested first using 2D PIV to verify the device's operation and to determine the extent to which the produced vortices could be maintained downstream. One camera was placed parallel to the flow viewing the region around the outlet of the device and another in a similar orientation to observe the region immediately downstream of that of the first camera. This allowed the degree of dissipation of the vortices to be observed after they had travelled a fixed distance.

The 2D data from the near camera at the outlet of the vortex tube is compiled in Appendix A grouped by the speed setting of the wind tunnel at which each dataset was obtained. Since a small portion of the vortex tube was visible within the near camera frame during data collection, approximately 12 mm^2 (0.0186 in^2) of invalid or missing data is present where the overlap occurred, centered at the vertical location of the outlet $y = 0$. All numerical data has been presented at the same scale as data of the same type. The first four figures present instantaneous data from the median camera frame that is representative of their associated datasets; the graphs presented throughout this chapter are included in these figures. In each of the streamline graphs, 300 random points were used to generate the streamlines. The final two figures in Appendix A present the time-averaged data from the same datasets. The downstream 2D camera view data is organized similarly in Appendix B.

It is important to note that the maximum speed at which the laser could operate was too slow to capture time-resolved particle image data from the vortex structures, since they manifest and travel at smaller timescales than the PIV apparatus is capable of operating at. Thus time-averaging the vorticity data could not produce meaningful results due to this timescale issue as

well as the turbulent nature of the vortices, and instead only the instantaneous vorticity data is presented. It is also important to note that the vorticity maps from the 2D images present the vorticity in the *z*-direction, i.e. negative normal to the camera, since only *x* and *y* data is available in these images.

As discussed in Chapter 4, in order to correctly perform the correlation calculations, the time interval between two consecutive frames must be small enough to observe the flow particles with a small but still measurable displacement. This leads to difficulty in obtaining accurate measurements when observing a slow-moving vortex core in a high speed freestream flow, or a high speed vortex core in a slow freestream flow. In this study observation of the vortex was prioritized and a value for *dt* was selected to ensure accurate measurement of the vortex core. In addition to Table 2 and Table 3 in Chapter 4, this value is shown in each of the individual graphs in the aforementioned appendices.

2D Velocity Maps, Vectors and Streamlines

Several results are immediately apparent from the instantaneous 2D data. The streamline graphs indicate that the vortices entrain the freestream flow to a much greater extent when the difference in velocity between the vortex core and freestream is large. This is most evident in the 40 psi & 3% wind tunnel setting, for which the velocity map is presented below in Figure 16. In this configuration, near the outlet of the vortex generator the majority of the vortex possesses a velocity approximately 20 m/s faster than the surrounding flow. The corresponding streamlines for this configuration are shown in Figure 17, where it can be clearly seen that the freestream is entrained into the vortex due to the significantly higher velocity of the vortex structure.

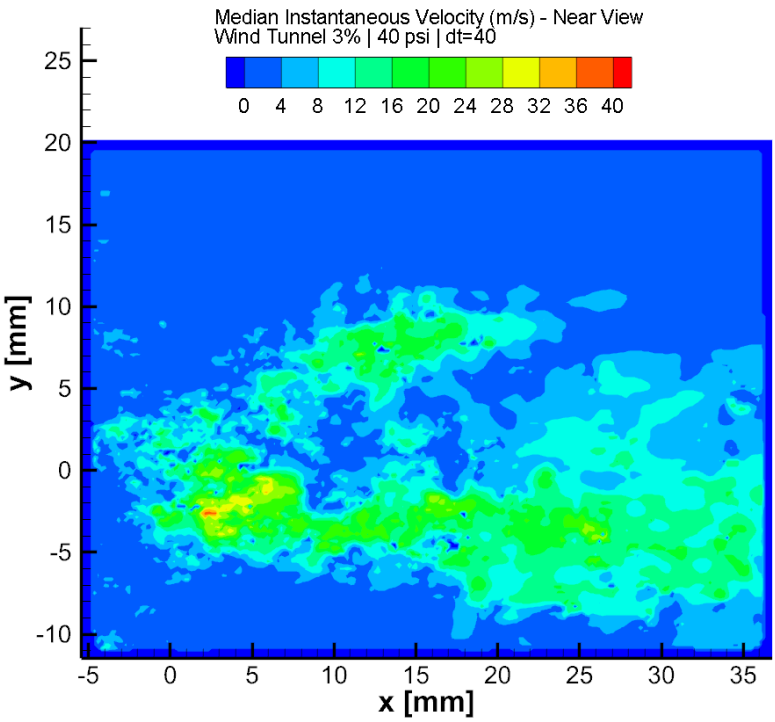

Figure 16: Instantaneous Near Region Velocity Map for 40 psi, 3% Wind Tunnel Setting

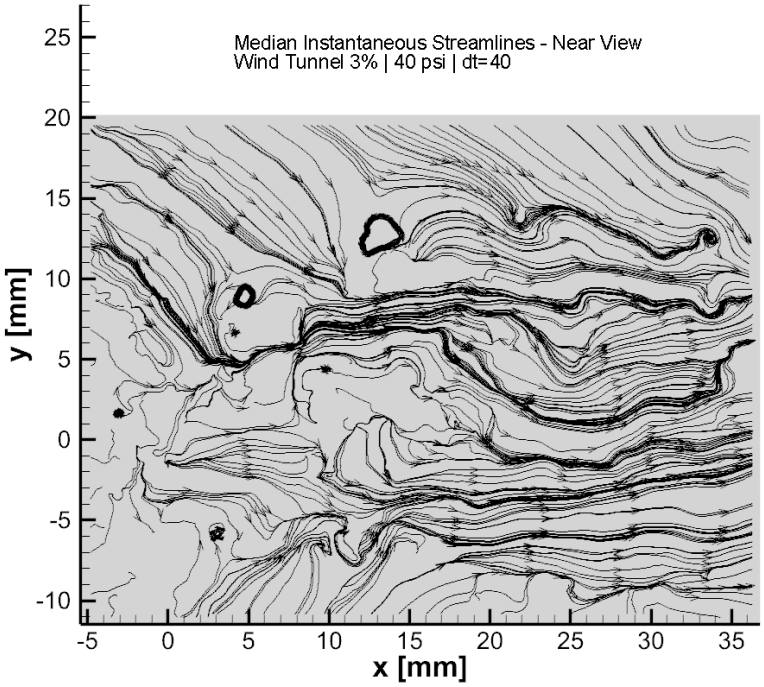

Figure 17: Instantaneous Near Region Streamlines for 40 psi, 3% Wind Tunnel Setting

By contrast, the velocity map and streamlines from a configuration with similar velocities in the freestream and vortex structures shows that entrainment is greatly reduced when the vortex

structure velocity is greater than the freestream velocity, but this difference in velocity is small. A prime example of this is the 20 psi & 20% wind tunnel setting, shown in Figure 18.

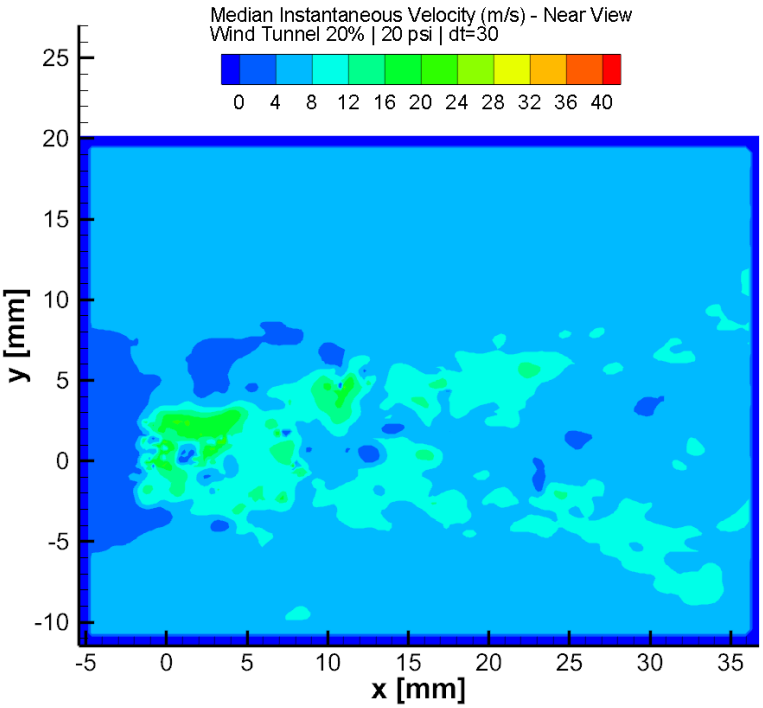

Figure 18: Instantaneous Near Region Velocity Map for 20 psi, 20% Wind Tunnel Setting

In this configuration the freestream flow is only slightly influenced by the presence of the vortex structure, as evidenced by the corresponding streamlines presented in Figure 19. While it may also be inferred that high speed flows generally entrain the vortices to a lesser degree than flows at lower speeds, this hypothesis is complicated by the varying degree of entrainment of freestreams by the vortices at different pressure settings. This is discussed further in the tomographic data analysis section.

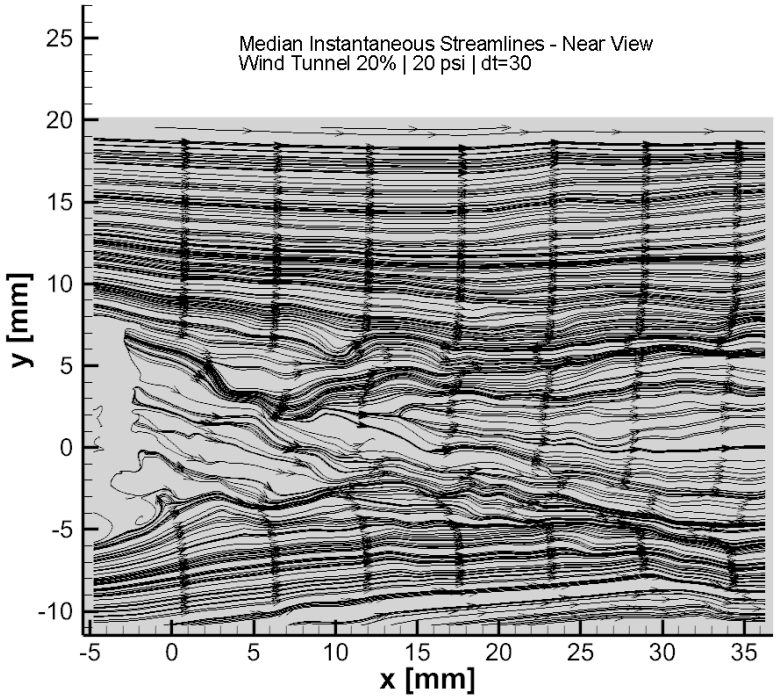

Figure 19: Instantaneous Near Region Streamlines for 20 psi, 20% Wind Tunnel Setting

Additionally, several small vortices and circulation areas in the *xy*-plane can be seen throughout the vortex structure in Figure 17 above, primarily in the upper portion of the graph, which may indicate the location of an annular portion of the vortex structure perpendicular to the camera, i.e., with its centerline extending in the *z*-direction. Also present to varying degrees in the corresponding vorticity maps, these circulation regions also appear frequently in the other 2D and 3D streamline graphs, most obviously in the 30 psi and 20% setting streamlines shown in Figure 20, which indicate the presence of an annular structure formed immediately after the outlet of the vortex generator.

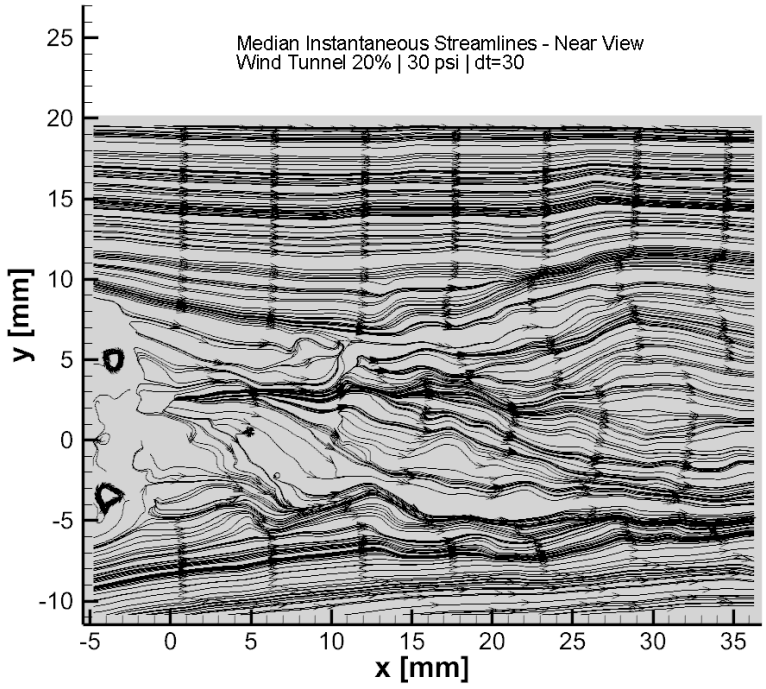

Figure 20: Instantaneous Near Region Streamlines for 30 psi, 20% Wind Tunnel Setting

As expected, from the velocity maps it can be observed that the vortices are rotating more quickly at higher pressures, since both the top and bottom of the vortex structures are more visible in the instantaneous data from configurations with 40 psi settings.

The downstream data from the vortex tube test is compiled in Appendix B. Due to a smudge or lens imperfection a small linear distortion is visible in nearly all velocity datasets at approximately x = 35 mm (1.378 inches), and another small distortion centered near x = 30 mm (1.181 inches), y = -7 mm (-0.276 inches) is also visible in the vorticity data. Most notable in these datasets is that the vortex structures remain intact further downstream for configurations in which the exit velocity of the vortex tube is much larger than the freestream velocity. In both the instantaneous and time-averaged velocity maps, the vortices produced at the 20 psi pressure setting have largely dissipated before entering the frame of the downstream camera, whereas at

the 40 psi pressure setting the central region of the vortices are still clearly visible. However, the downstream vortices maintain their average velocity for longer at the 20% setting.

In the instantaneous downstream data the turbulent nature of the vortices is more noticeable than in the near camera view data. As previously discussed in this chapter, since the camera timing is not synchronized to the period of the vortices, the motion of the vortex structures cannot be followed frame-by-frame. However, the instantaneous images still show the vortices at various orientations as they spiral downstream; this is most noticeable in the 20 psi and 5% wind tunnel speed configuration, shown in Figure 21. The corresponding velocity vectors further illustrating this spiral motion are shown in Figure 22.

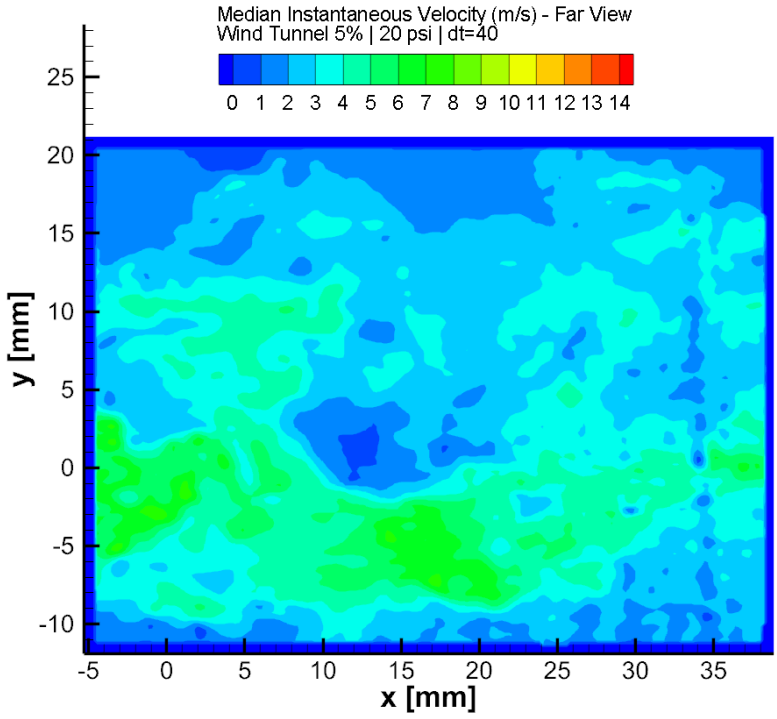

Figure 21: Instantaneous Downstream Velocity Map for 20 psi, 5% Wind Tunnel Setting

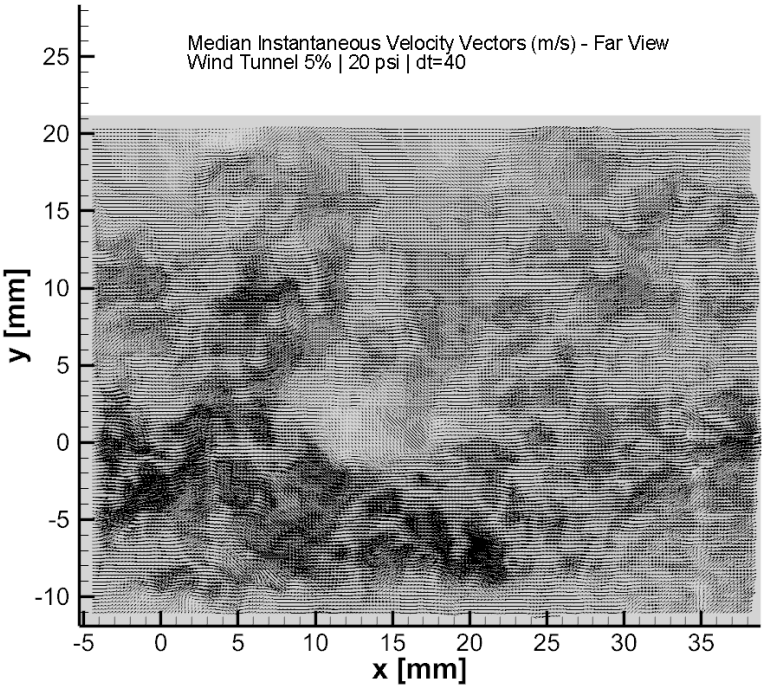

Figure 22: Instantaneous Downstream Velocity Vectors for 20 psi, 5% Wind Tunnel Setting

2D z-Vorticity Maps

The vorticity in the *x*-direction cannot be observed in 2D testing in which the cameras are facing the negative *z*-direction, but *z*-vorticity data can still be used to draw conclusions about the flow behavior. Figure 23 shows the *z*-vorticity map from the near camera from the 40 psi and 5% configuration, the velocity map of which is shown in Figure 24, and Figure 25 shows the corresponding downstream vorticity. In the near map it can be seen that the regions with high-magnitude *z*-vorticity correspond to the high-velocity regions from the outlet of the vortex generator as seen in Figure 24. In particular, the location of the region centered at approximately (0, 3) mm or (0, 0.118) inches in Figure 23 matches part of a high-velocity region in Figure 24. This vorticity is likely produced by a previously discussed annular portion of the vortex structure. Similarly, vorticity regions in Figure 25 indicate the downstream presence of a vortex structure near (30, -5) mm or (1.181, 0.197) inches in this same flow configuration.

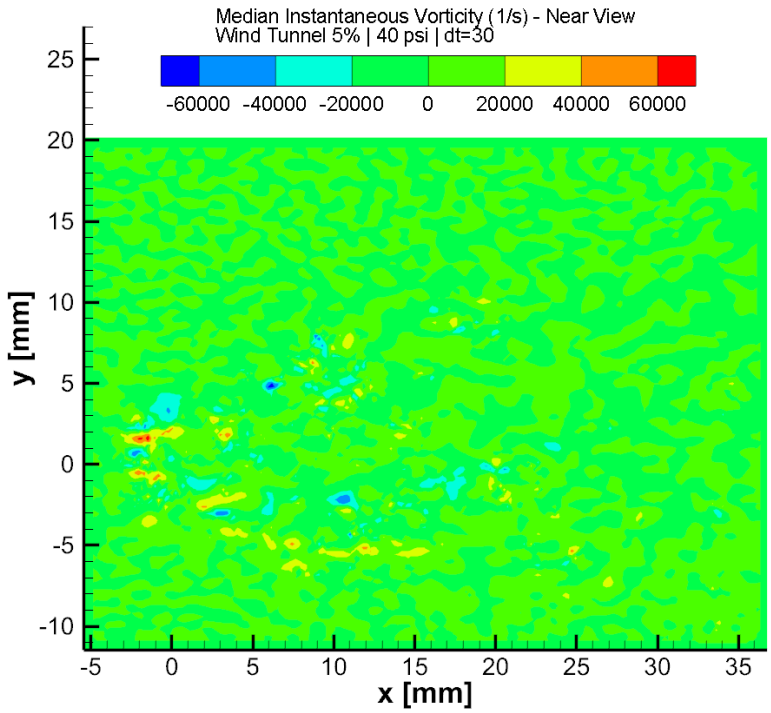

Figure 23: Instantaneous Near Region Vorticity Map for 40 psi, 5% Wind Tunnel Setting

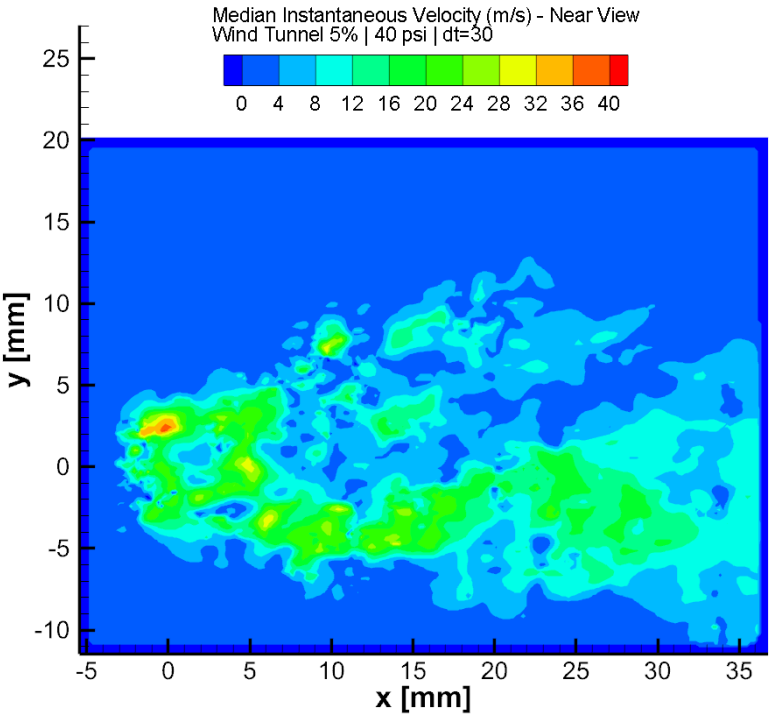

Figure 24: Instantaneous Downstream Velocity Map for 40 psi, 5% Wind Tunnel Setting

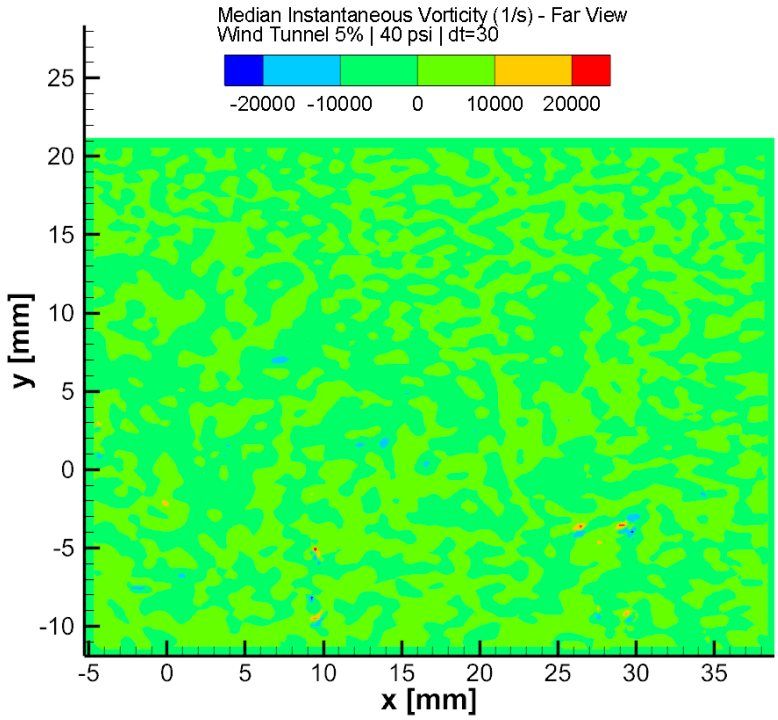

Figure 25: Instantaneous Downstream Vorticity Map for 40 psi, 5% Wind Tunnel Setting

3D Tomographic Test Results Overview

After the 2D PIV testing was complete, tomographic testing was performed to observe the vortex structures with more detail. Since the tomographic approach only allows for a limited region to be observed, the available PIV hardware apparatus was focused on the outlet region, and further downstream behavior of the vortices was not observed simultaneously. The vortex generator was operated in the same configurations as with the 2D analysis, and the laser apparatus was modified to illuminate a 70 mm (2.755 inches) long, 10 mm (0.398 inches) thick and 50 mm (1.969 inches) tall volume immediately following the outlet. Four PIV cameras were then positioned to observe this region from multiple orientations to produce the images to be used for tomographic reconstruction. It is important to note that the orientation of the vortex tube in the wind tunnel causes the produced vortex to have a positive vorticity in the *x*-direction.

The tomographic data is compiled in Appendix C, wherein the vortex behavior is much more clearly visible than in the 2D datasets. As with the 2D data, the 3D instantaneous data is shown for the median camera frame followed by the time averaged data. Also shown are the instantaneous Q-criterion isosurfaces for the median camera frame colored by velocity magnitude. The instantaneous velocity vectors show the circulatory motion at several planes along the length of the tomography volume much more readily than the 2D views, and further support the conclusion that when the vortex velocity is greater than that of the freestream, the difference in velocity between the vortex and freestream is the primary factor in maintaining vortex structures in the flow. Note that the locations of the planes at which data is presented are constant for all graphs.

After completing this analysis, a final set of tomographic tests was performed to observe the interaction of the vortices with a NACA 0012 swept airfoil with an aspect ratio of $AR = 4$ and an angle of attack of 5°. The airfoil was placed 6 inches downstream from the vortex tube to prevent the wake from the generator apparatus from interfering with the vortex-airfoil interaction. The vortex generator was positioned at the same elevation as the airfoil, and slightly offset from the wingtip such that the outside of the vortex tube was tangent to the vertical plane of the airfoil wingtip. While not ideal for detecting wingtip vortex dissipation, this was done to allow the laser to be projected on the upper surface of the airfoil rather than on the wingtip. Centering the laser volume over the wingtip would have caused the edge of the airfoil to produce significant glare in each of the tomographic camera views, which was avoided by moving the laser volume slightly spanwise inward over the airfoil such that the edge of the airfoil was just outside the laser volume. The resulting data is compiled in Appendix E, in which the control data gives the behavior of the airfoil without the vortex generator present. Due to the orientation of

the laser, only data from above the airfoil could be obtained, and additional measurement apparatus or an alternative setup would be required to measure both the top and bottom surfaces. While insightful, these tests were primarily intended to demonstrate the capability of the vortex generator rather than produce a sizable dataset to work with, and additional testing will be required to fully verify the results of the AFRL simulation.

3D Tomographic Velocity Data and Streamlines

A prime example of the aforementioned significance of velocity difference is the contrast between the graphs of instantaneous velocity vectors with the wind tunnel set to 3% and the vortex tube operating at 20 psi, and the wind tunnel set to 20% with vortex tube pressure of 20 psi, shown in Figures 26 & 27, respectively.

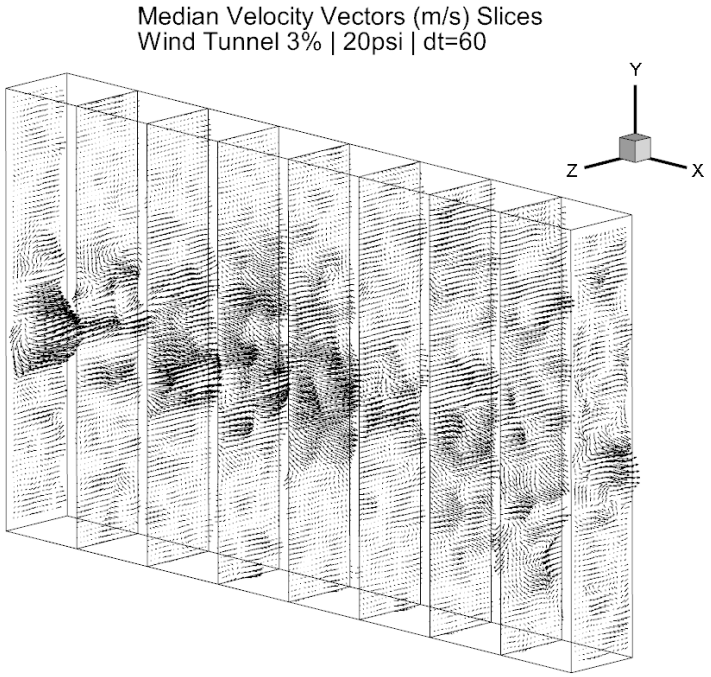

Figure 26: Instantaneous Velocity Vectors Slices for 20 psi, 3% Wind Tunnel Setting

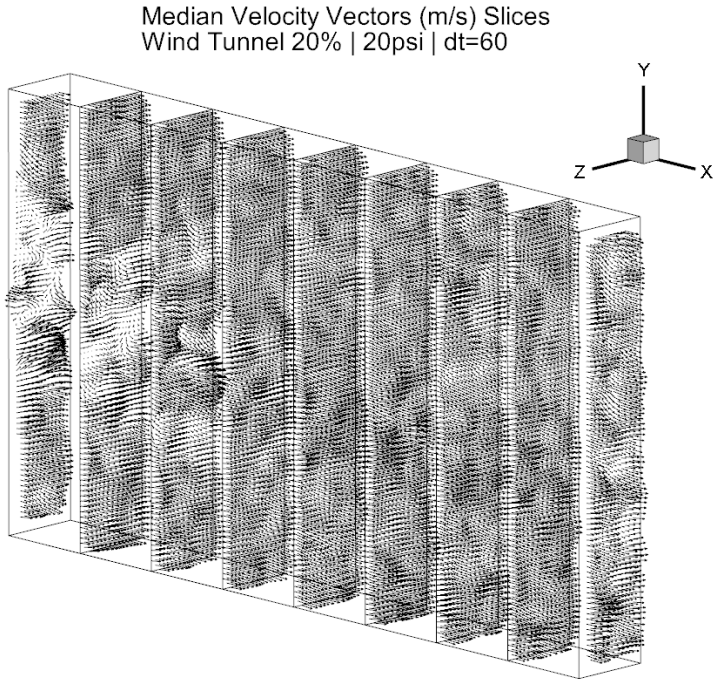

Figure 27: Instantaneous Velocity Vector Slices for 20 psi, 20% Wind Tunnel Setting

At the 3% setting, the vortex pattern and circulatory motion can be seen prominently in the first five slices starting from the -*x* bound, where the outlet is positioned. However, at the 20% setting the vortex is harder to distinguish from the freestream due to the similar velocities. As demonstrated in the 2D datasets, this results in the corresponding downstream vortices remaining intact longer at the 3% setting than 20%. The difference is less visible at the 40 psi setting, since the velocity of the vortex is still high enough to maintain the vortex structures regardless of the selected freestream velocity.

The corresponding velocity map slices of the 3% and 20% wind tunnel settings with pressure of 20 psi are shown in Figures 28 & 29, respectively. These graphs also demonstrate that the vortex is notably more visible at the slower 3% setting due to the difference in velocity being greater than in the 20% setting. This does not only facilitate qualitative observation of the vortices, it also leads to increased entrainment of the freestream flow by the faster vortex core, as

demonstrated in the 2D data and illustrated in Figure 30 by the streamlines for the 20 psi and 3% configuration.

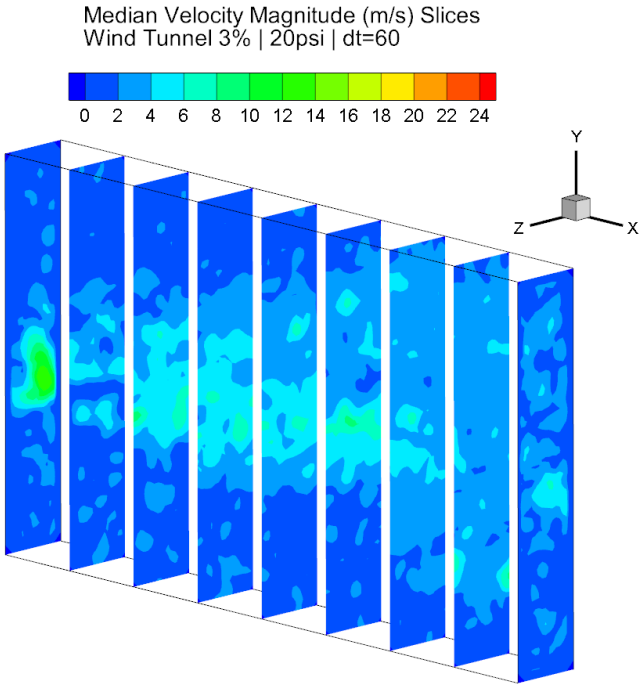

Figure 28: Instantaneous Velocity Vectors Slices for 20 psi, 3% Wind Tunnel Setting

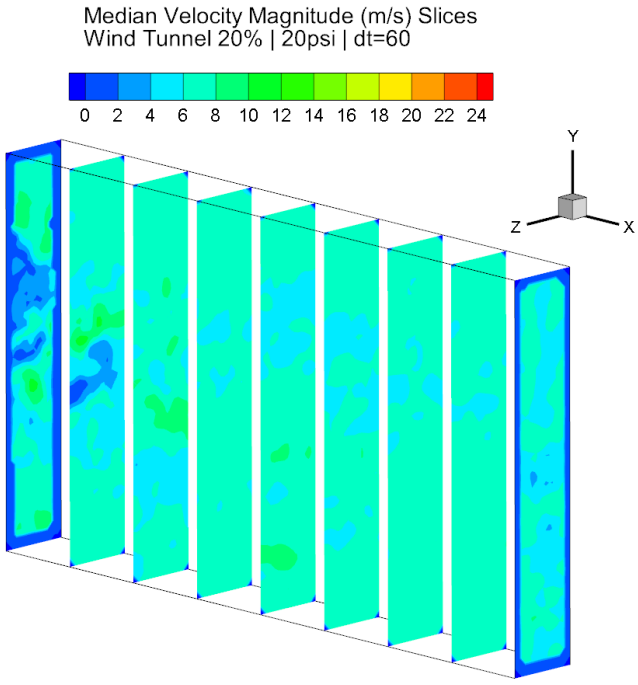

Figure 29: Instantaneous Velocity Vector Slices for 20 psi, 20% Wind Tunnel Setting

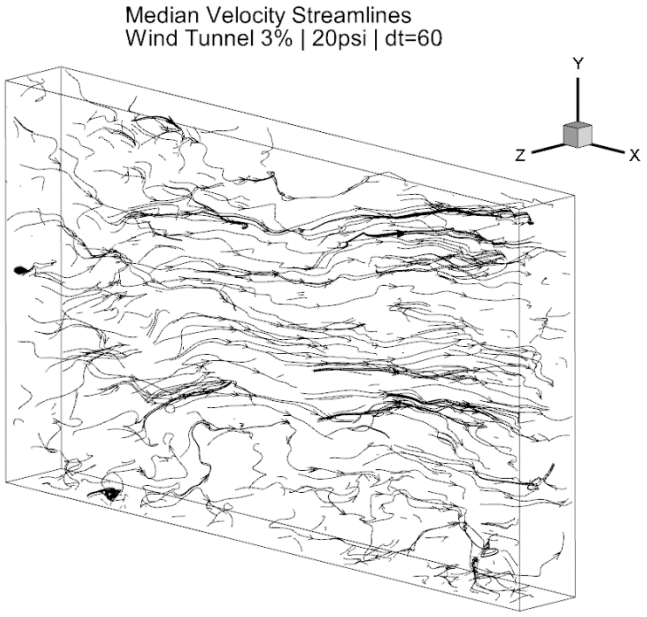

Figure 30: Instantaneous Velocity Vectors Slices for 20 psi, 3% Wind Tunnel Setting

3D Tomographic x-Vorticity and Q-Criterion Analysis

For comparison with the AFRL simulation's incident vortex, the Q-criterion isosurfaces of each tomographic dataset are presented in Appendix D for Q = 5 and with velocity magnitude presented as color. For locating vortex structures, simply calculating vorticity isosurfaces can be misleading since vorticity regions may arise outside of the vortex structure, such as near walls, and identification based on low pressure regions may not be adequate for large or complex flows with widely varying pressures. [13] A better approach is the Q-criterion, developed by Hunt, Wray and Moin [14] which gives the second invariant of the velocity tensor, and provides a more accurate means of locating vortex cores. This derived value is calculated from the following equation:

$$Q = \frac{1}{2}(\|\Omega^2\| - \|S^2\|) \qquad \text{(Eq. 8)}$$

where Ω is the vorticity magnitude and S is the strain rate magnitude. In order to use this equation the region of calculation must possess a pressure lower than that of the freestream. The

isosurfaces of this criterion represent regions in which the vorticity magnitude is a specific amount greater than the strain rate magnitude. [15] Flow visualization using the Q-criterion is dependent on the value of *Q* chosen for the isosurfaces and as such can be somewhat arbitrary, and while other methods of identifying vortex cores are available, the Q-criterion was chosen for ease of comparison with the AFRL simulation since a value of $Q = 5$ was already specified for visualization of the incident vortex.

Before measuring the Q-criterion directly, some insight can be gained by observing the x-vorticity map of the 40 psi and 3% configuration in Figure 31. In most of the high-vorticity regions, a corresponding region with the opposite sign can be seen nearby, suggesting that entrained counter-rotating flow is present, as mentioned in the discussion of the 2D data. This counter-rotation is included in the calculation of the Q-criterion, since it is the magnitude of the vorticity that is being considered, but the presence of the vortex core is still understood since it is the cause of the entrainment.

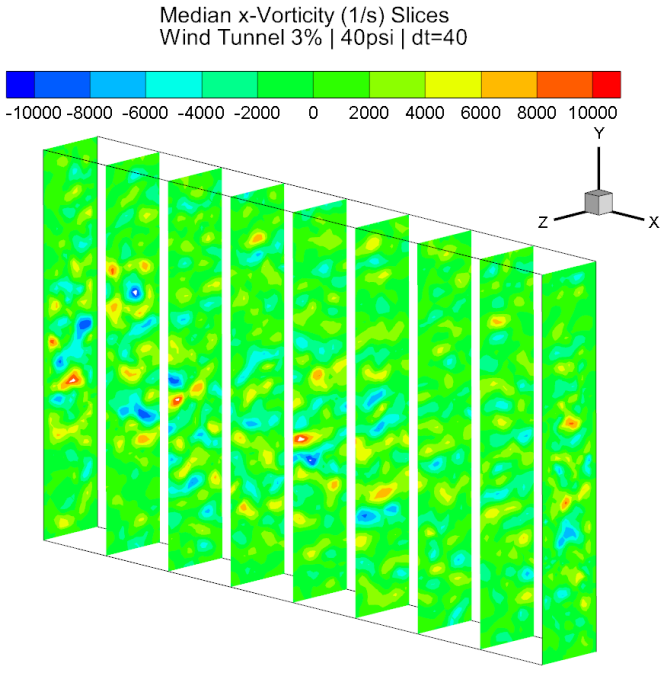

Figure 31: Instantaneous Velocity Vector Slices for 20 psi, 20% Wind Tunnel Setting

Despite the heavy noise due to turbulence, it can be deduced that the vortex core maintains its strength further downstream when the freestream velocity is low, while at higher freestream velocities the vortex core is weakened more quickly. As seen below in Figure 32, the vortex core is most visible in the $Q = 5$ isosurfaces graph of the 40 psi and 3% wind tunnel configuration.

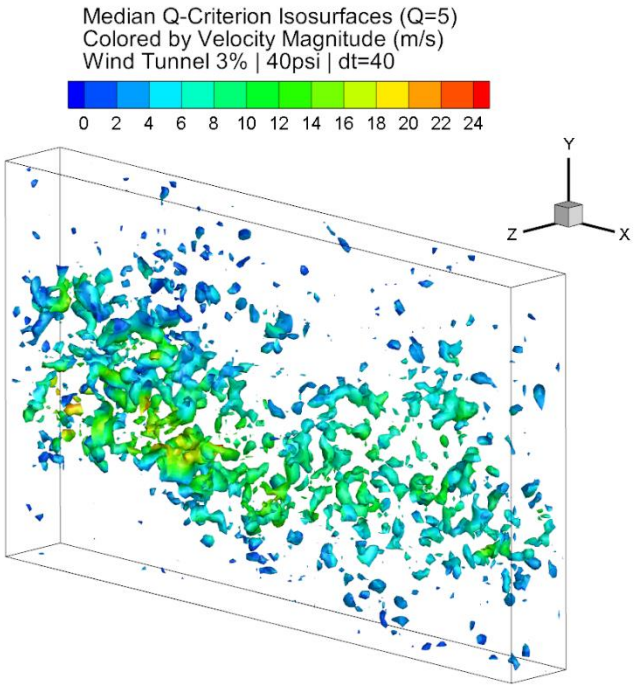

Figure 32: Instantaneous Q-Criterion Isosurfaces for 40 psi, 3% Wind Tunnel Setting

The dissipation rate of the vortices was also evaluated from the tomographic data, which allowed a solution to be obtained for the problem of insufficient 2D data for time-averaging vorticity. As previously discussed, since the measurement process is not time-resolved to the vortex structures, accurate time-averaged vorticity calculations cannot be performed on the structures themselves. However, the time-averaged vorticity magnitude in an *x*-plane in the tomography region can be used to determine the average strength of the vortices that pass through that plane during the measurement process. Unlike the use of time-averaging to identify

vortex structures, which is unmanageable with different timescales, this application does not rely on the location of the vortex within the *x*-plane. Rather, the calculation is only concerned with the magnitude of the vorticity of the structures, therefore the difference in timescales is not a limitation in determining the average strength of vortices over the measurement time.

The maximum and minimum vorticity magnitudes at each of the *x*-planes in previous graphs are presented in Figures 33 through 36. As previously mentioned, the design of the vortex tube led to the production of outlet flow with positive *x*-vorticity, and as such the negative values in the below graphs are likely the result of entrained counter-rotating flow circulating behind the vortex structures.

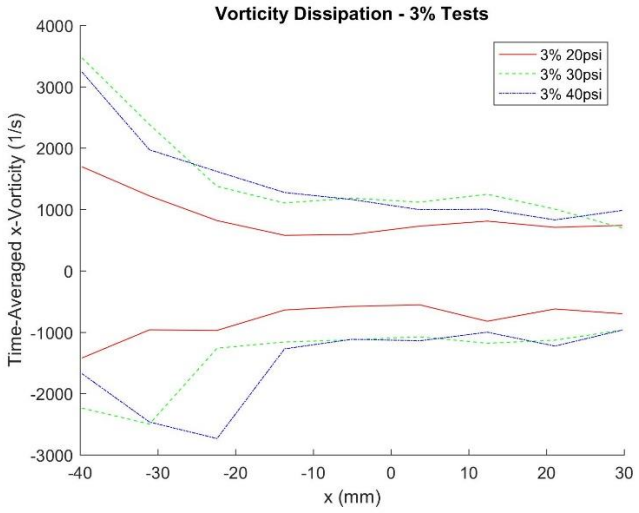

Figure 33: Vortex Dissipation through Tomography Region for 3% Wind Tunnel Setting

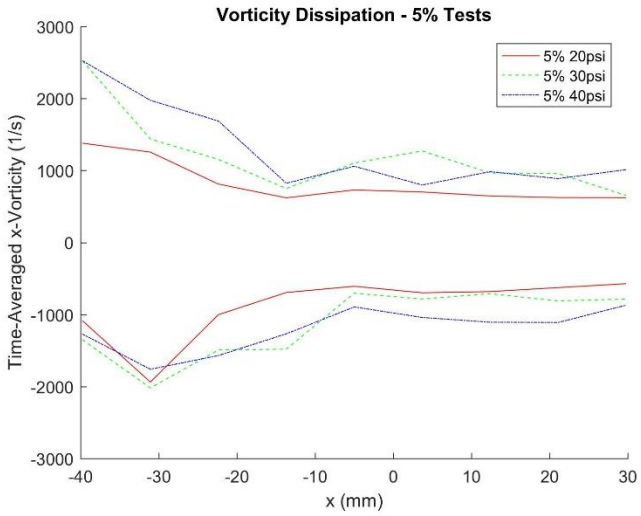

Figure 34: Vortex Dissipation through Tomography Region for 5% Wind Tunnel Setting

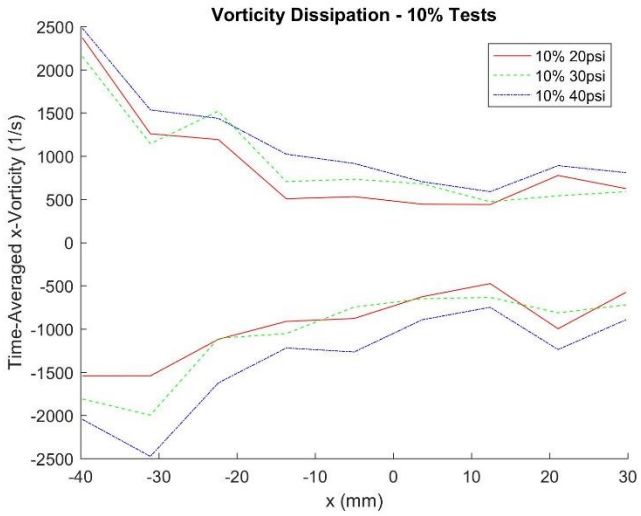

Figure 35: Vortex Dissipation through Tomography Region for 10% Wind Tunnel Setting

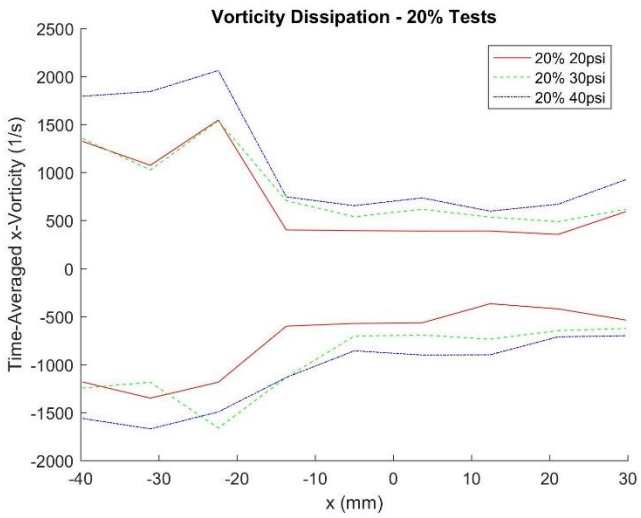

Figure 36: Vortex Dissipation through Tomography Region for 20% Wind Tunnel Setting

The dissipation rate of the produced vortices with respect to downstream distance can be visualized more clearly through the use of numerical *x*-derivatives obtained from the positive maximum vorticity measurements. Several deductions can be made from Figures **37** through **40** in which these derivatives are plotted. It can be seen that at lower freestream wind tunnel velocities the vortices dissipate over a greater distance than at higher speeds, and when a higher supply pressure is combined with the faster freestream velocities, the vortices experience greater fluctuation in strength further downstream. The vorticity derivative magnitudes also begin to decrease more significantly approximately 30 mm (1.181 inches) after the vortex generator outlet, thus the trend in vorticity magnitude is nonlinear.

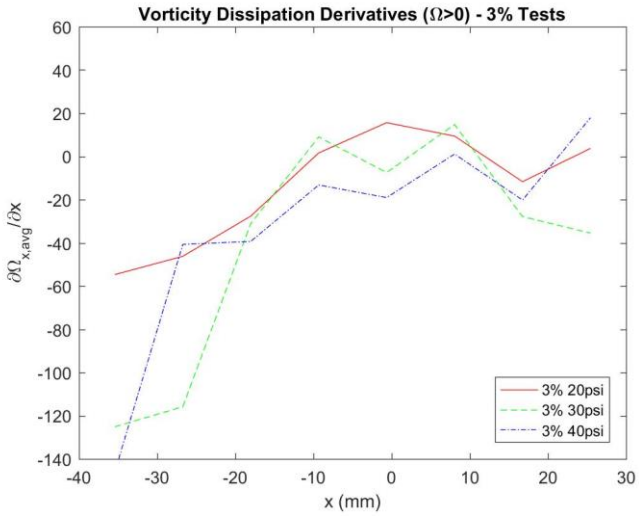

Figure 37: Vortex Dissipation Numerical x-Derivative for 3% Wind Tunnel Setting

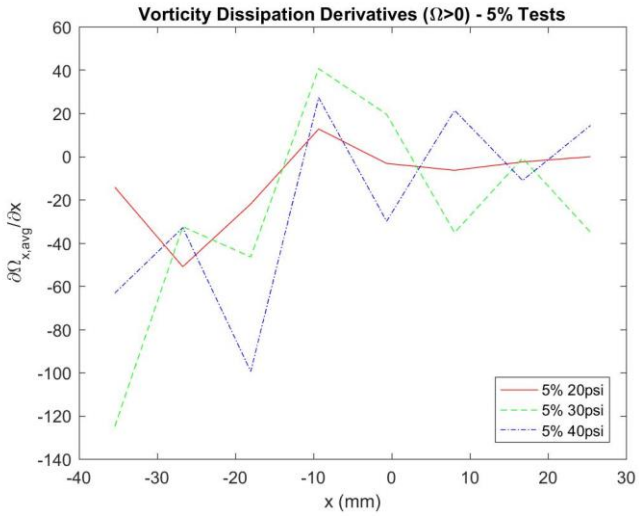

Figure 38: Vortex Dissipation Numerical x-Derivative for 5% Wind Tunnel Setting

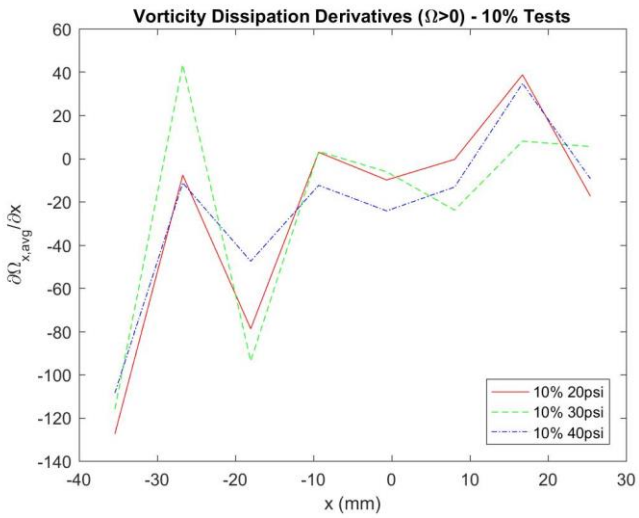

Figure 39: Vortex Dissipation Numerical x-Derivative for 10% Wind Tunnel Setting

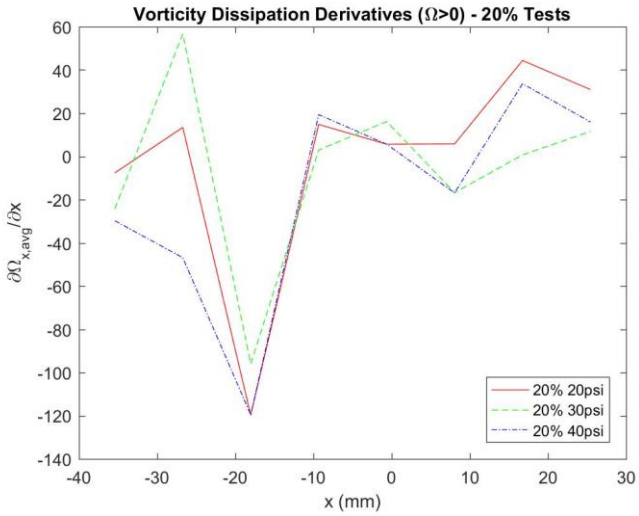

Figure 40: Vortex Dissipation Numerical x-Derivative for 20% Wind Tunnel Setting

Data from the 2D tests indicate that the difference in velocity between the freestream and vortex leads to increased entrainment and keeps the vortex structure intact as it travels downstream. By contrast, from this 3D vorticity data it can be deduced that the difference in velocity also causes the strength of the vortex to drop off more quickly in the region immediately following the outlet. Thus in high velocity flows with lower vortex tube pressure settings, despite the structures persisting longer in the flow, their strength is reduced as a side effect of the

velocity difference. Tables **4** and **5** below summarize the produced vorticity at the vortex generator outlet and at the maximum *x*-value of the tomography region.

Table 4: Maximum Time-Averaged Vorticity Measurements at Vortex Generator Outlet

Ω (1/s)	**3%**	**5%**	**10%**	**20%**
20 psi	1695.210	1379.880	2368.070	1325.320
30 psi	3470.530	2523.750	2152.670	1354.960
40 psi	3239.890	2524.980	2479.220	1794.040

Table 5: Maximum Time-Averaged Vorticity Measurements at Maximum *x*-Value

Ω (1/s)	**3%**	**5%**	**10%**	**20%**
20 psi	739.689	623.144	624.112	593.548
30 psi	696.067	653.810	588.809	617.909
40 psi	984.326	1012.160	808.438	926.641

3D Airfoil Interaction Test Velocity Data

After obtaining the tomographic data presented in the last sections, a final set of tests was performed to observe the interaction of the generated vortices with a downstream airfoil. Each of these tests was performed with the wind tunnel set to 5% strength, and the position of the NACA 0012 airfoil was not modified during or between tests. This wind tunnel setting was selected based on previous test data with the goal of maintaining vortex strength far enough downstream for the interaction to be measurable. The laser volume was slightly larger than the previous tests at approximately 105 mm (4.134 inches) in the *x*-direction, 65 mm (2.559 inches) in the *y*-direction, and 10 mm (0.393 inches) in the *z*-direction. The timing of the laser and cameras was

set to a constant value of $dt = 40$ μs. As with the previous graphs, the median timestep is used to present representative instantaneous data.

Before testing the vortex-airfoil interaction, a control test was performed with the airfoil placed in the freestream without the vortex generator present, to establish how the flow behaved around the airfoil without influence from the vortex tube. The median velocity maps and corresponding vectors of this test are shown below in Figures 41 and 42, respectively. As expected, the airfoil causes minimal interruption to the flow, while the region of increased velocity in the second-to-last x-plane is likely the result of a random disturbance of the wind tunnel freestream flow. Time-averaging this velocity data gives a similar impression, and the averaged graphs are included in Appendix E. As alluded to by these graphs, it should be noted that since the laser is projected onto the upper surface of the airfoil, the region below the airfoil cannot be observed since the seeder particles are traveling through the airfoil's shadow.

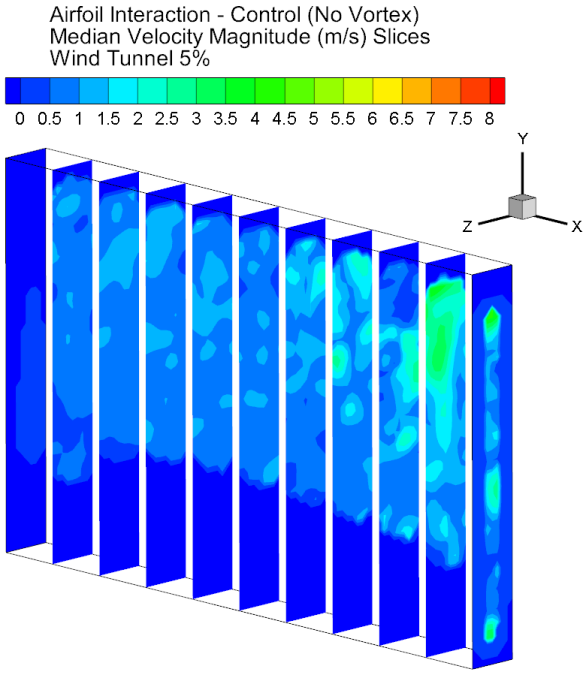

Figure 41: Airfoil Interaction Control Median Velocity Maps

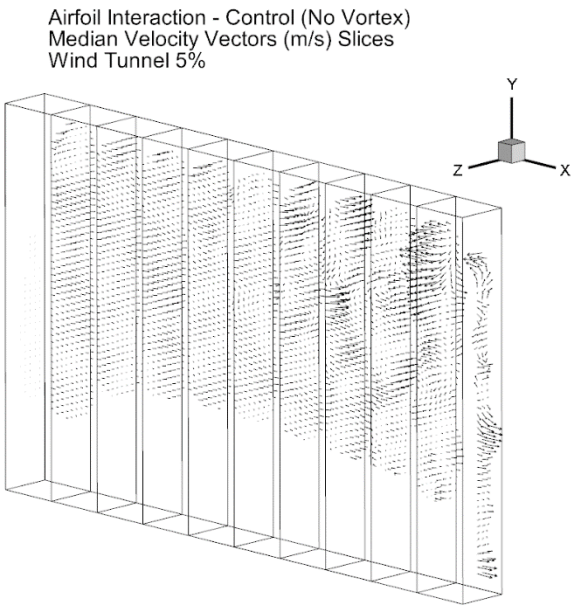

Figure 42: Airfoil Interaction Control Median Velocity Vectors

With the inclusion of the vortex tube at the 20 psi setting, the presence of the vortex near the surface of the airfoil is immediately noticeable. As discussed in the review of the AFRL simulation, the splitting of the vortex over the two airfoil surfaces can be observed in Figure 43.

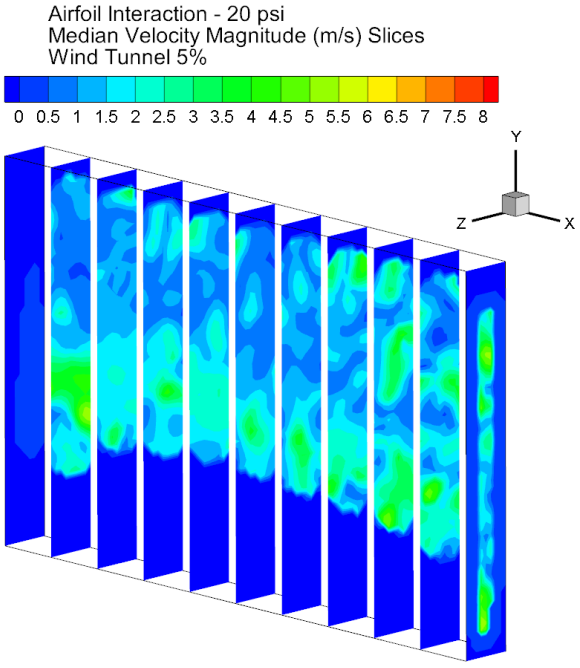

Figure 43: Airfoil Interaction Median Velocity Maps for Vortex Generator, 20 psi

However, when increasing the pressure setting of the vortex tube, the interaction is less visible due to the expansion of the generated vortex after traveling downstream. This problem is evident in the velocity maps of the 30 psi setting but is especially visible at the 40 psi setting, shown in Figure 44, where the vortex has already expanded to fill much of the observed volume. Thus in future tests a balance must be found between avoiding the effects of the apparatus wake and maintaining the vortex further downstream. Despite the disruption of flow throughout the volume, the time-averaged velocity maps such as that of Figure 45 for the 40 psi setting indicate that the faster-moving vortex core is still reaching the leading edge of the airfoil, though its strength has been diminished during the expansion of the vortex.

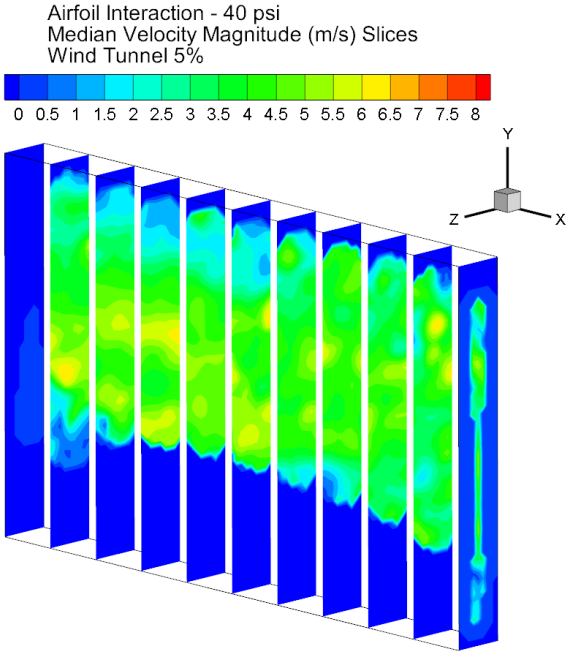

Figure 44: Airfoil Interaction Median Velocity Maps for Vortex Generator, 40 psi

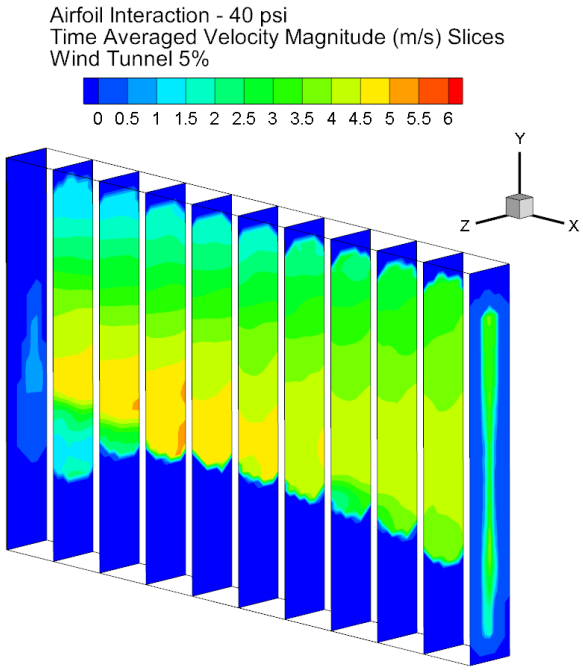

Figure 45: Airfoil Interaction Average Velocity Maps for Vortex Generator, 40 psi

3D Airfoil Interaction Test Vorticity Data

The presence of the vortex core at the surface of the airfoil was further analyzed using by calculating the x-vorticity of the flow field for each test, and the resulting graphs are included in Appendix E. However, since the vortices had already dissipated and expanded considerably before reaching the observed volume, these graphs were of limited use in analyzing the vortex interaction with the airfoil. The most useful of these graphs is shown in Figure 46, which is the vorticity data for the 30 psi setting. Here the regions of relatively high vorticity are scattered throughout the flow field, and although one such region is present near the leading edge of the airfoil, the vorticity has already decreased so significantly that it is difficult to identify the path of the vortex core over the airfoil with this method, thus the Q-criterion was used to obtain a better representation of the vortex interaction with the airfoil.

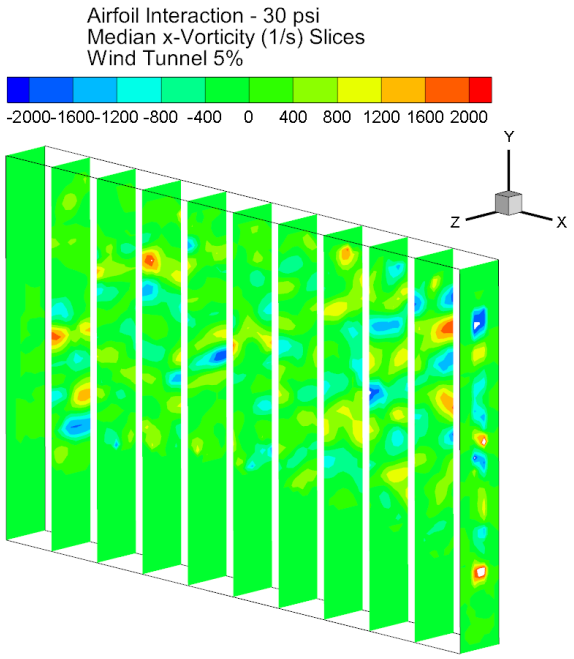

Figure 46: Airfoil Interaction Median x-Vorticity Maps for Vortex Generator, 30 psi

The Q-criterion was evaluated in a similar manner to the previous tomographic tests, but due to the decreased strength of the vortices a lower value of $Q = 0.5$ was used when graphing the isosurfaces. Also included in Appendix E are isosurfaces of $Q = 0$ to present the condition of the flow after the vortices have dissipated. This value of Q indicates regions in which the vorticity and strain rate are equal, and as such these isosurfaces are located throughout the flow field due to the absence of high-strength vortices. As presented in Figure 47, data from the control test established that minimal vorticity was present at the surface of the airfoil in the absence of the vortex generator.

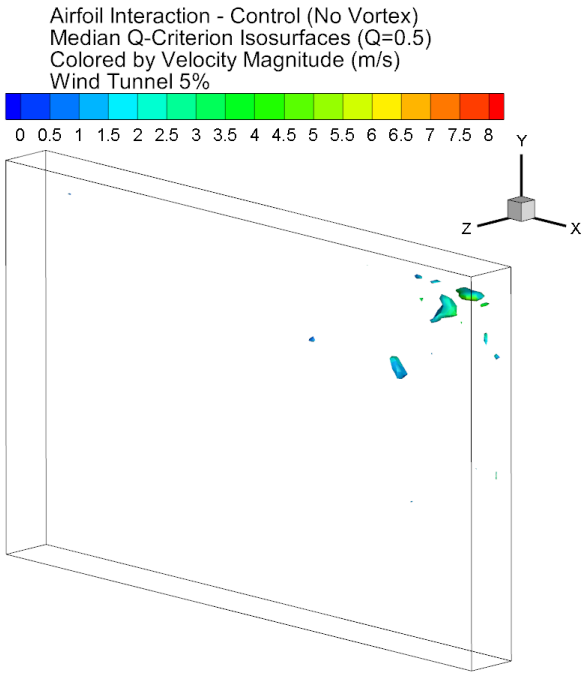

Figure 47: Airfoil Interaction Control Median Q-Criterion Isosurfaces

With the inclusion of the vortex generator at 20 psi, the effect of the vortex begins to take shape, but the 30 and 40 psi settings, shown in Figures 48 and 49, respectively, more clearly illustrate the influence of the vortex on the airfoil boundary layer. Similarly to the velocity data, the isosurfaces present upstream of the leading edge of the airfoil indicate that the vortex is being split over the airfoil and maintaining at least a part of its vorticity as it does so. This agrees with the AFRL simulation's description of the behavior of the incident vortex after sweeping spanwise across the airfoil, even though this test did not involve movement of the vortex generator.

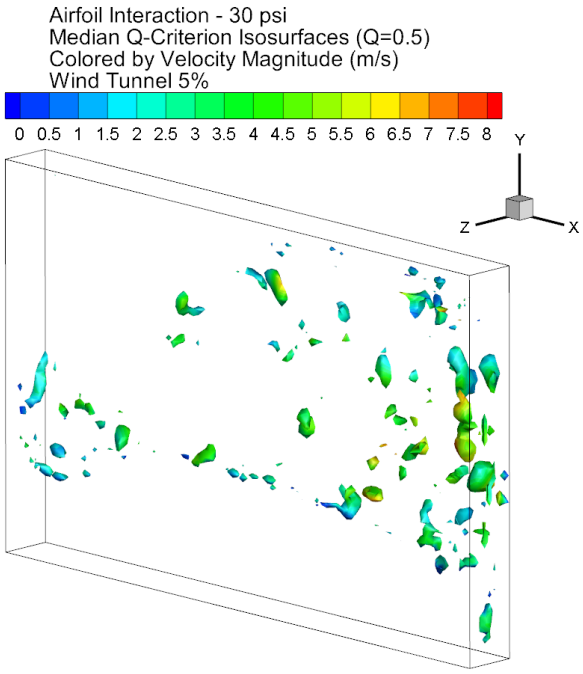

Figure 48: Airfoil Interaction Median Q-Criterion Isosurfaces for Vortex Generator, 30 psi

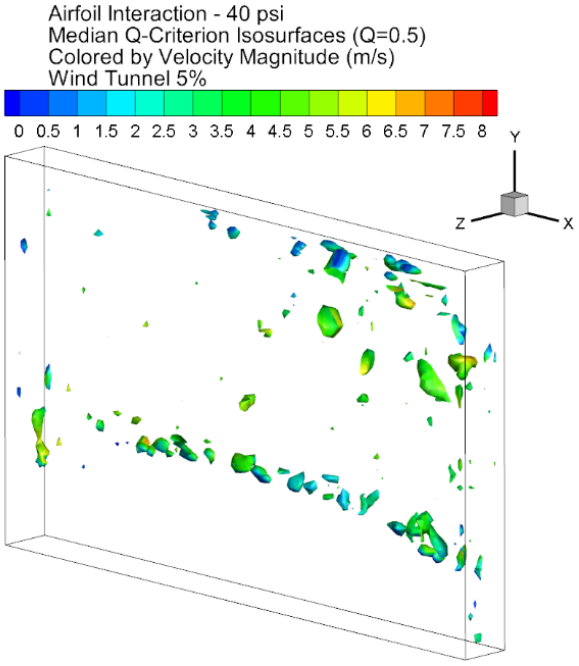

Figure 49: Airfoil Interaction Median Q-Criterion Isosurfaces for Vortex Generator, 40 psi

CHAPTER 6: CONCLUSION

In this study the suitability of a pressurized vortex tube for the generation of streamwise vortices was examined. The device was operated with compressed air supplied at various pressures in a wind tunnel at various freestream velocities, and the produced vortices were observed using 2D and tomographic PIV. Data from these tests indicate that increasing the air supply pressure improves the strength of the vortex at the exit of the device and allows the structures to be maintained more consistently further downstream. When the vortex velocity is greater than that of the freestream flow, a large difference in velocity between the vortex and freestream also contributed to keeping the vortex structure intact, while increasing entrainment of the freestream flow. By contrast, near the outlet vortex strength is dissipated faster with a larger difference in velocities. Low freestream velocities also reduced the degree of dissipation of the vortices after the initial reduction and allowed the vortex cores to retain their strength after traveling downstream. The relation between vorticity and travel distance was observed to be nonlinear due to significant reduction in vorticity near the outlet, followed by a more gradual decline in vortex strength.

The AFRL simulation data indicates that an incident vortex vertically aligned and positioned spanwise along a downstream airfoil will split over both surfaces and maintain its vorticity after doing so. Limited testing of the generated streamwise vortices and a downstream airfoil produced data in agreement with this aspect of the simulation. However, the vortices in these tests had already lost a significant portion of their energy from traveling downstream before intersecting the airfoil, making accurate measurement more difficult than in the freestream interactions tests, and additional testing should be done to verify these results.

Future Work

Measurement of the generated vortices at higher wind tunnel velocities was restricted due to the limitations of the PIV measurement apparatus for capturing images of multiple flow regions at greatly differing velocities. This prevented the production of vortices in a freestream with characteristics more similar to the AFRL simulation, and also prevented time-resolved vortex data from being obtained. Future studies may resolve this hinderance through the use of faster laser and camera equipment, capable of operating at timescales closer to those of the vortex cores.

For a more thorough verification of the AFRL simulation, additional tests should be conducted analyzing the interaction of a generated streamwise vortex and a downstream airfoil. In such tests, increasing the distance between the vortex generator and the airfoil reduces the influence of the wake from the generator apparatus on the airfoil, but also leads to the strength of the vortex being diminished as it travels and expands. A balance must be found between avoiding the effects of the apparatus wake and maintaining the vortex further downstream. Additional insight into improving vortex uniformity may also be found from an analytical investigation of the vortex tube interior.

REFERENCES

[1] J. D. Anderson, Fundamentals of Aerodynamics, 6th ed., New York, NY: McGraw-Hill Education, 2017.

[2] NASA Glenn Research Center, "Downwash Effects on Lift," 2015. [Online]. Available: https://www.grc.nasa.gov/WWW/k-12/airplane/downwash.html.

[3] D. McLean, "Wingtip Devices: What They Do and How They Do It," in *Boeing Performance and Flight Operations Engineering Conference*, 2005.

[4] R. T. Whitcomb, "A Design Approach and Select Wind-Tunnel Results at High Subsonic Speeds for Wing-Tip Mounted Winglets," NASA Langley Research Center, Hampton, VA, 1976.

[5] S. Suranto Putro, S. Sutardi and W. Widodo, "Numerical Study of Aerodynamic Analysis on Wing Airfoil NACA 43018 with the addition of Forward and Rearward Wingtip Fence," in *Proceedings of the International Mechanical Engineering and Engineering Education Conferences*, 2016.

[6] Federal Aviation Administration, "Pilot and Air Traffic Controller Guide to Wake Turbulence," [Online]. Available: https://www.faa.gov/training_testing/training/media/wake/04sec2.pdf. [Accessed March 2020].

[7] P. B. S. Lissaman and C. A. Shollenberger, "Formation Flight of Birds," *Science*, pp. 1003-1005, 1970.

[8] T. Yang, L. Zhiyong, X. Neng, S. Yan and L. Jun, "Optimization of Positional Parameters of Close-Formation Flight for Blended-Wing-Body Configuration," *Heliyon,* 2018.

[9] M. S. G. Godard, "Control of a Decelerating Boundary Layer. Part 1: Optimization of Passive Vortex Generators," *Aerospace Science and Technology,* pp. 181-191, 2006.

[10] D. J. Garmann and M. R. Visbal, "Interactions of a streamwise-oriented vortex with a finite wing," *Journal of Fluid Mechanics,* pp. 782-810, 2015.

[11] S. Leibovich and K. Stewartson, "A sufficient condition for the instability of columnar vortices," *Journal of Fluid Mechanics,* pp. 335-356, 1983.

[12] M. Mohiuddin and S. Elbel, "A Fresh Look At Vortex Tubes Used As Expansion Device in Vapor Compression Systems," in *International Refrigeration and Air Conditioning Conference,* 2014.

[13] J. Jeong and F. Hussain, "On the identification of a vortex," *Journal of Fluid Mechanics,* pp. 69-94, 1995.

[14] J. Hunt, A. Wray and P. Moin, "Eddies, Streams, and Convergence Zones in Turbulent Flows," in *Proceedings of the 1988 Summer Program,* Stanford, CA, 1988.

[15] V. Kolář, "Vortex identification: New requirements and limitations," *International Journal of Heat and Fluid Flow,* pp. 638-652, 2007.

APPENDIX A: 2D PIV DATA FROM NEAR CAMERA

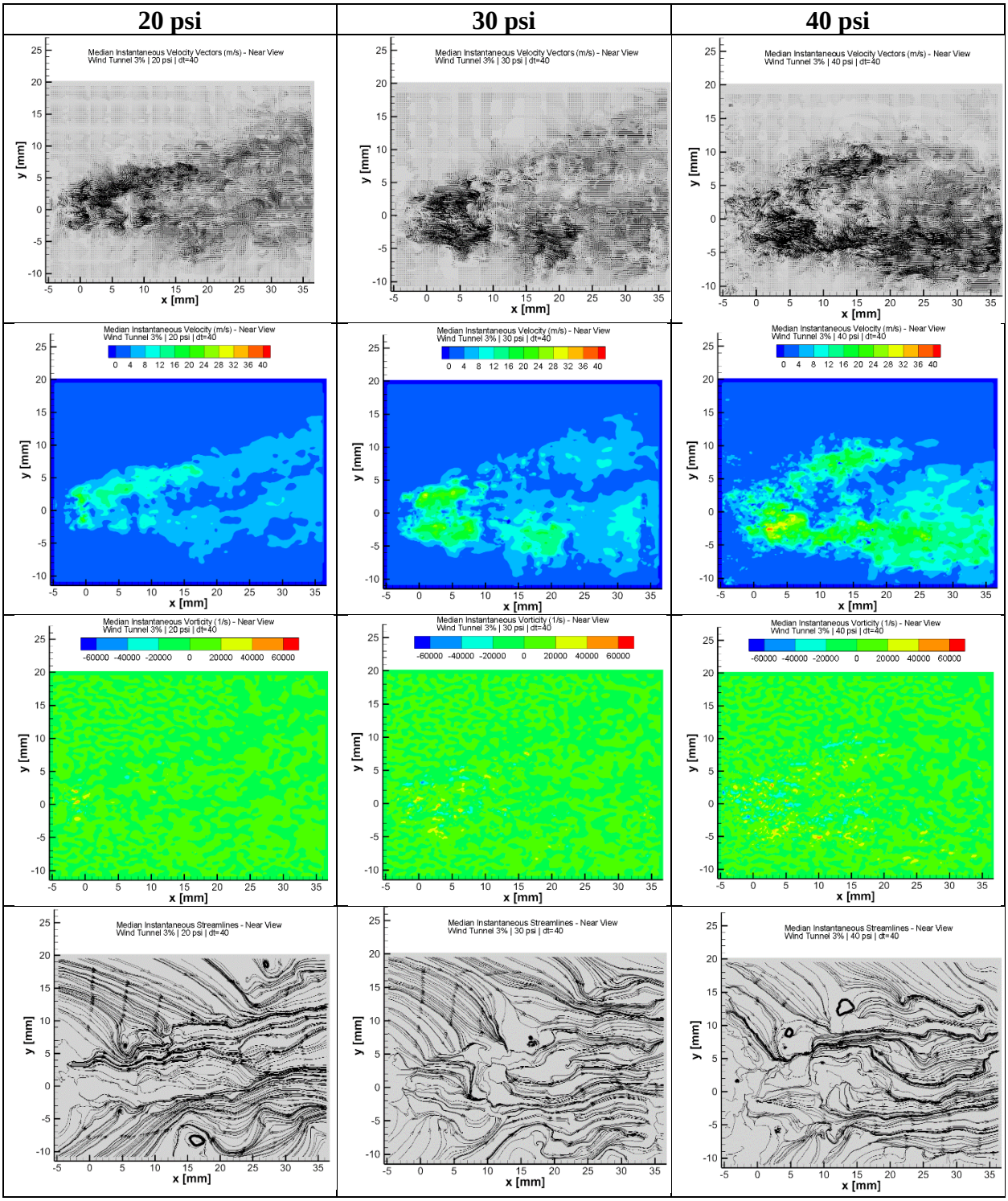

Figure A1: 2D Median Instantaneous Vortex Tube Near Data, 3% Wind Tunnel Speed

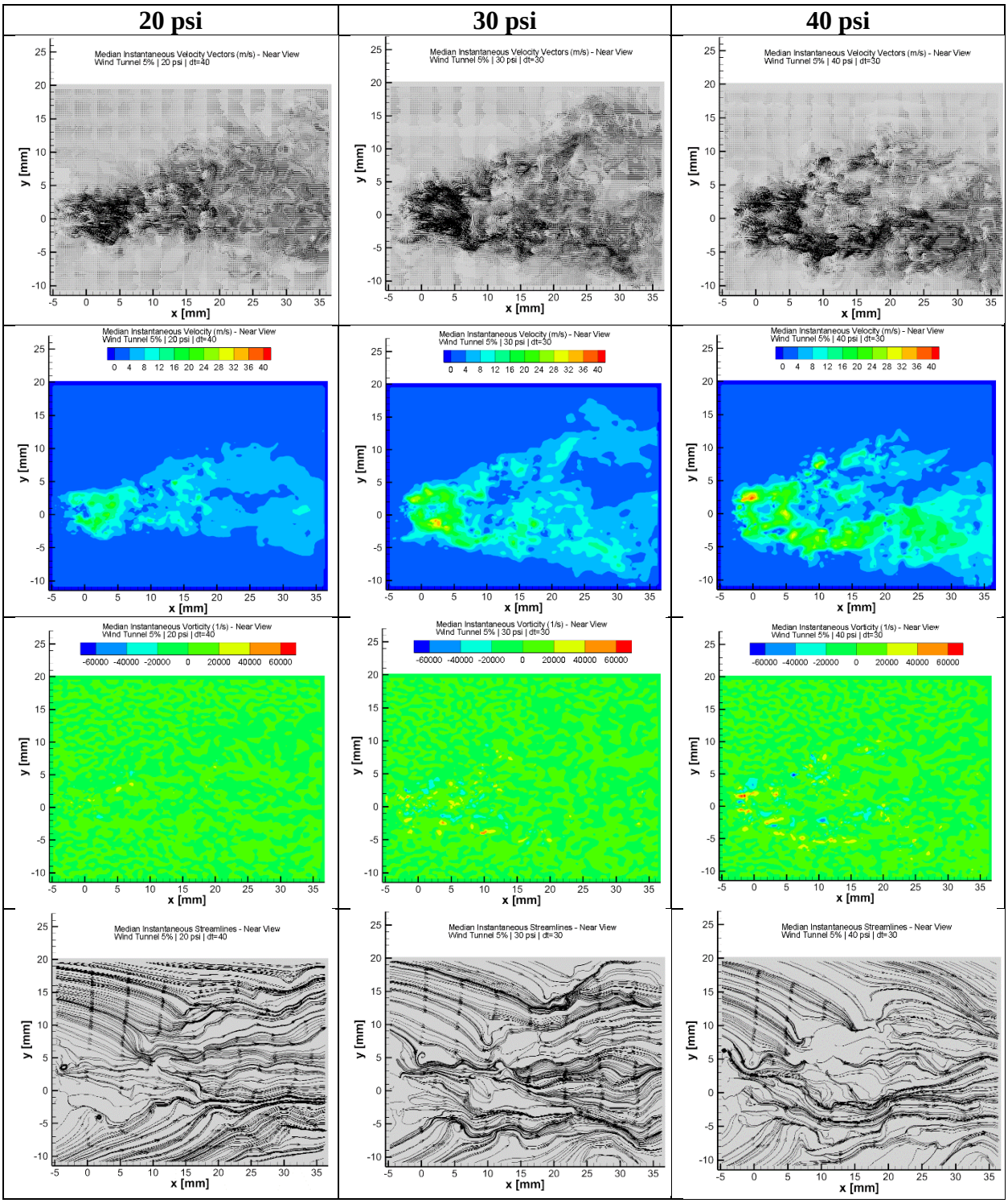

Figure A2: 2D Median Instantaneous Vortex Tube Near Data, 5% Wind Tunnel Speed

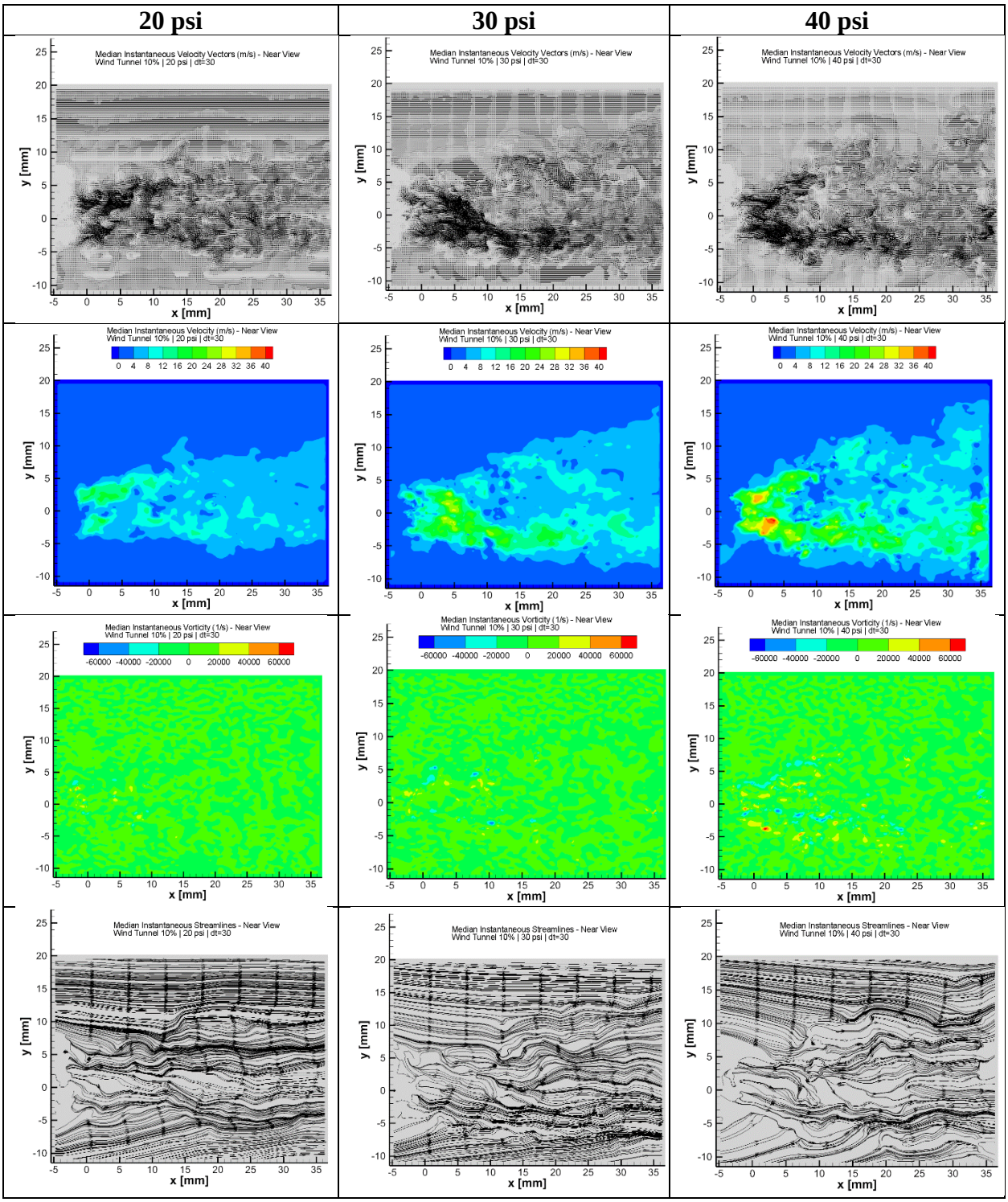

Figure A3: 2D Median Instantaneous Vortex Tube Near Data, 10% Wind Tunnel Speed

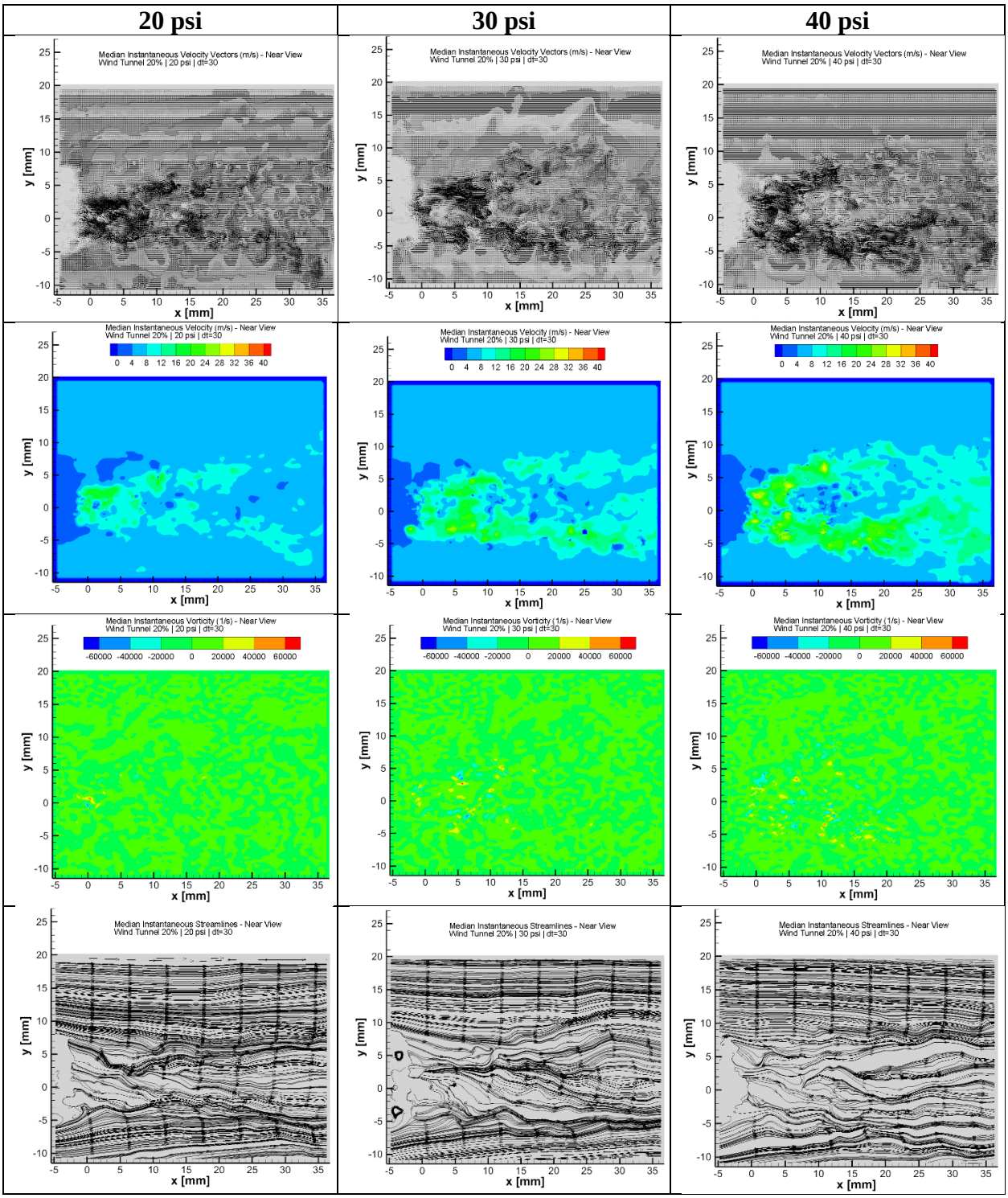

Figure A4: Median Instantaneous Vortex Tube Near Data, 20% Wind Tunnel Speed

	20 psi	30 psi	40 psi
3%	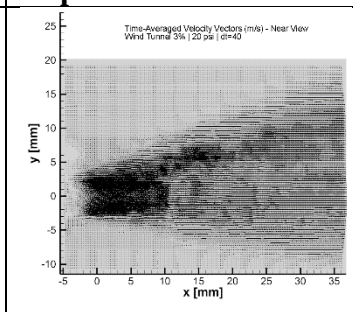	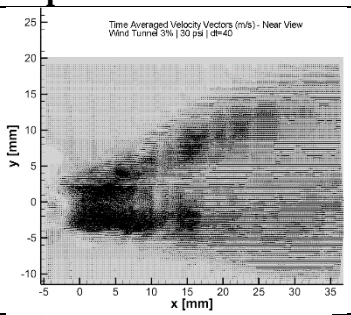	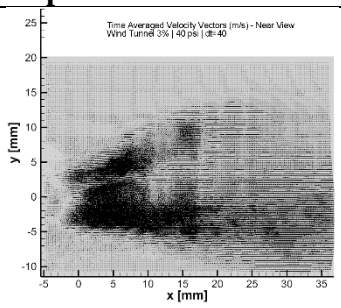
5%	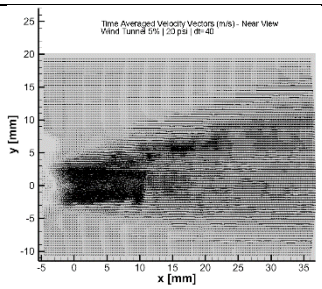	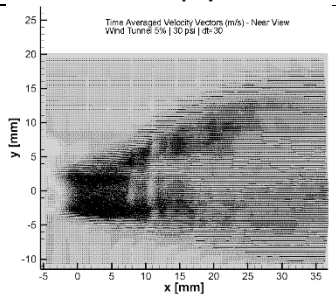	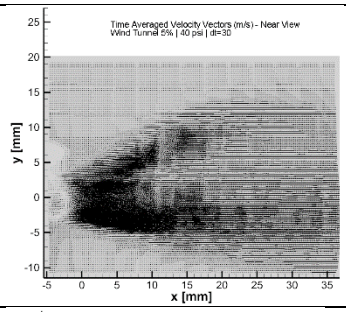
10%	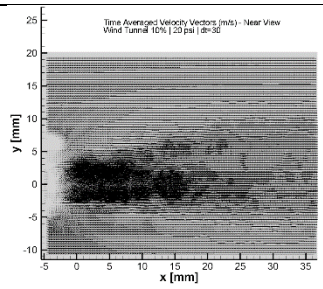	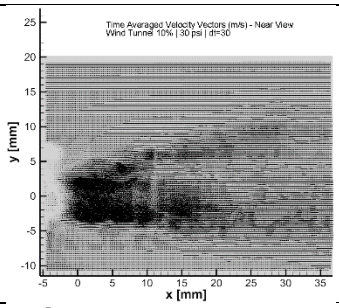	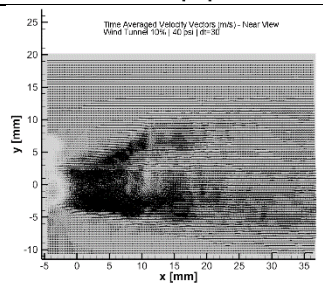
20%	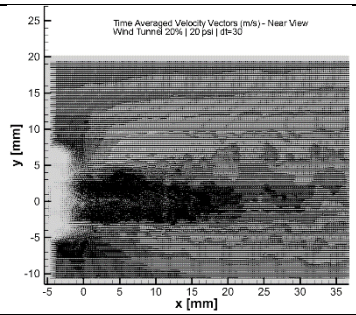	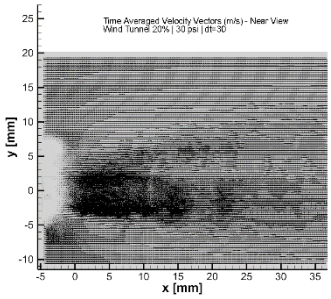	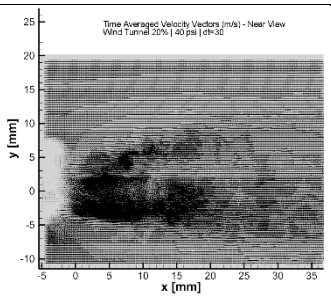

Figure A5: Time Averaged Vortex Tube Velocity Vectors from Near Camera

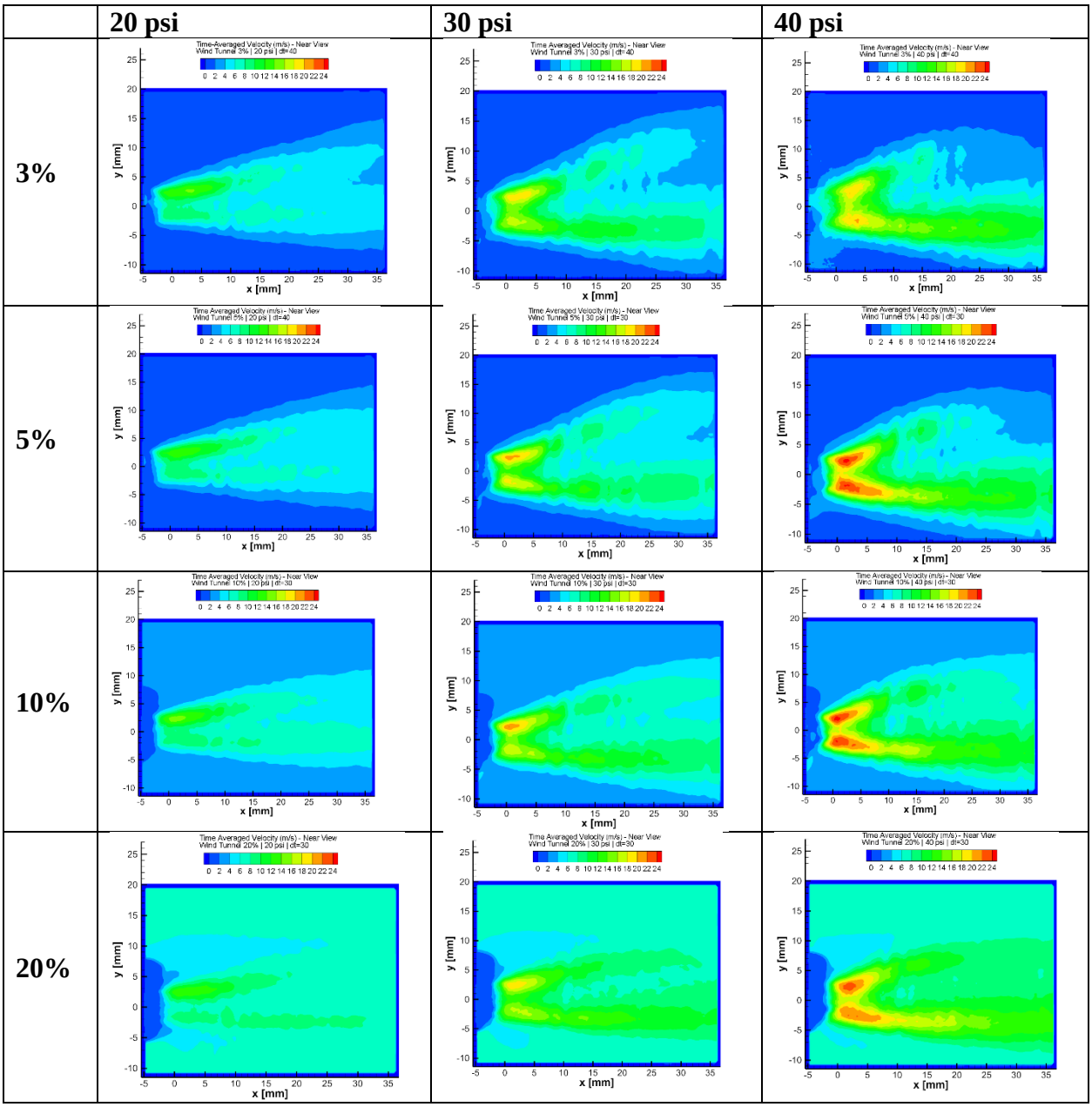

Figure A6: Time Averaged Vortex Tube Velocity Maps from Near Camera

APPENDIX B: 2D PIV DATA FROM DOWNSTREAM CAMERA

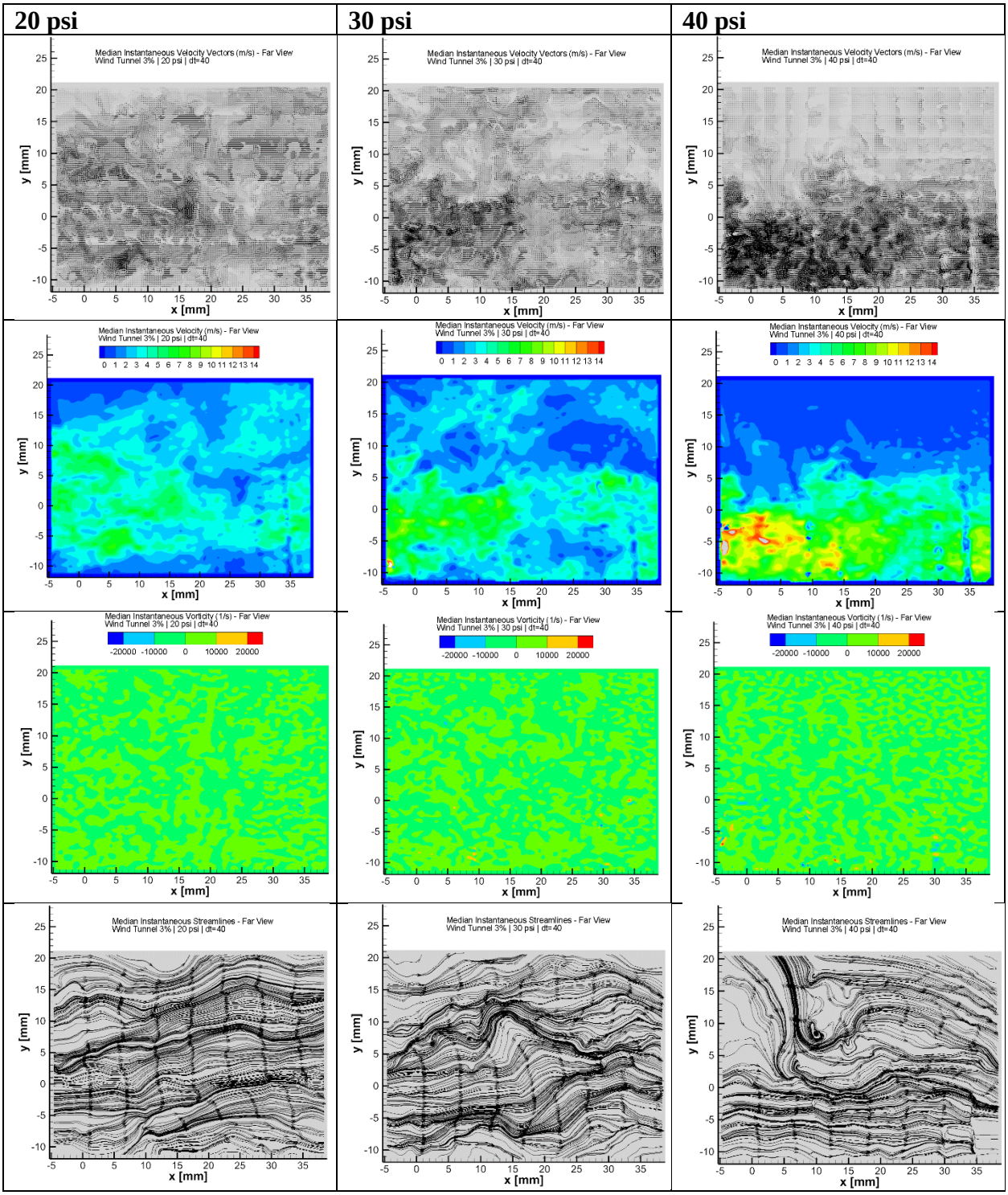

Figure B1: 2D Median Instantaneous Vortex Tube Downstream Data, 3% Wind Tunnel Speed

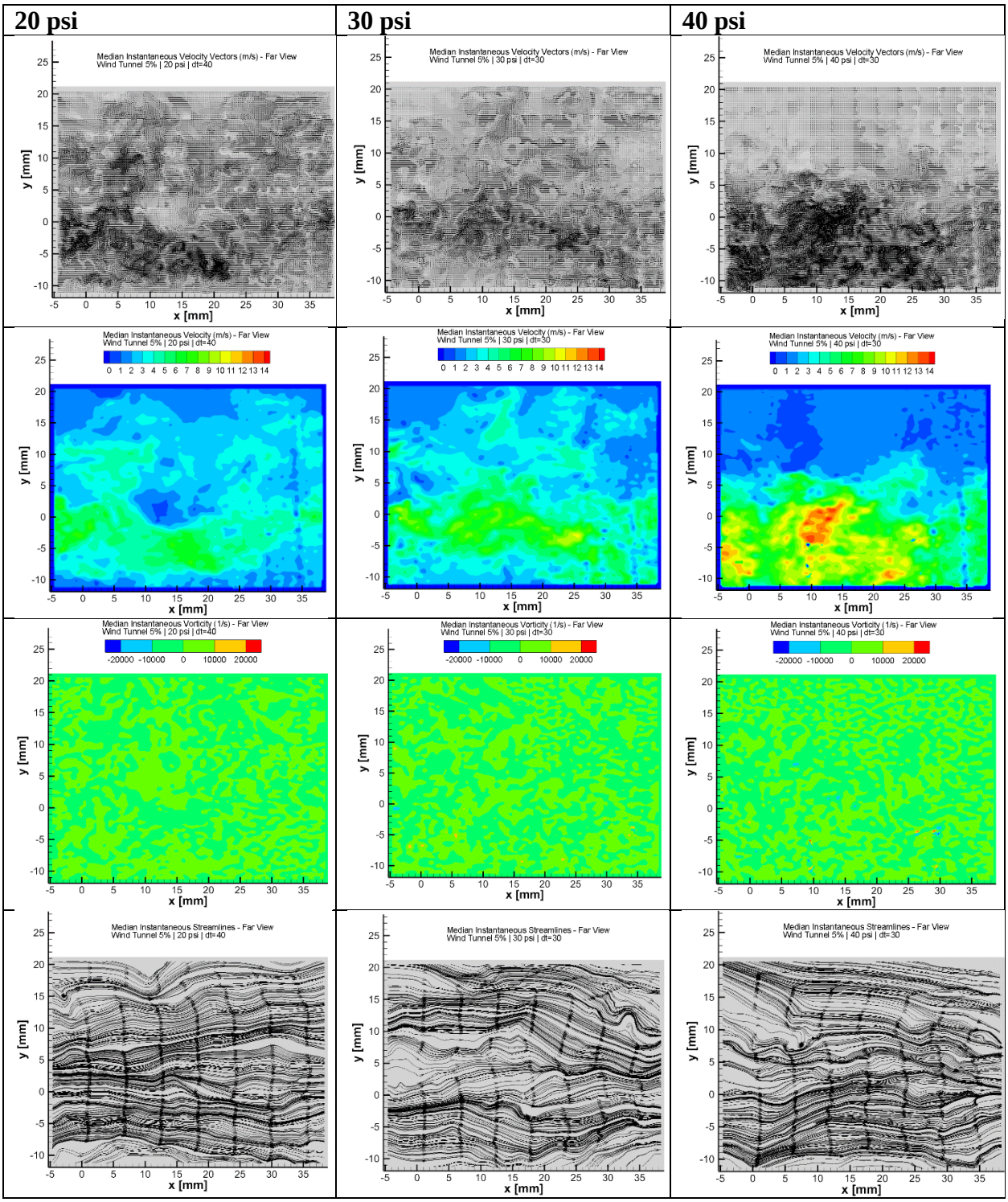

Figure B2: 2D Median Instantaneous Vortex Tube Downstream Data, 5% Wind Tunnel Speed

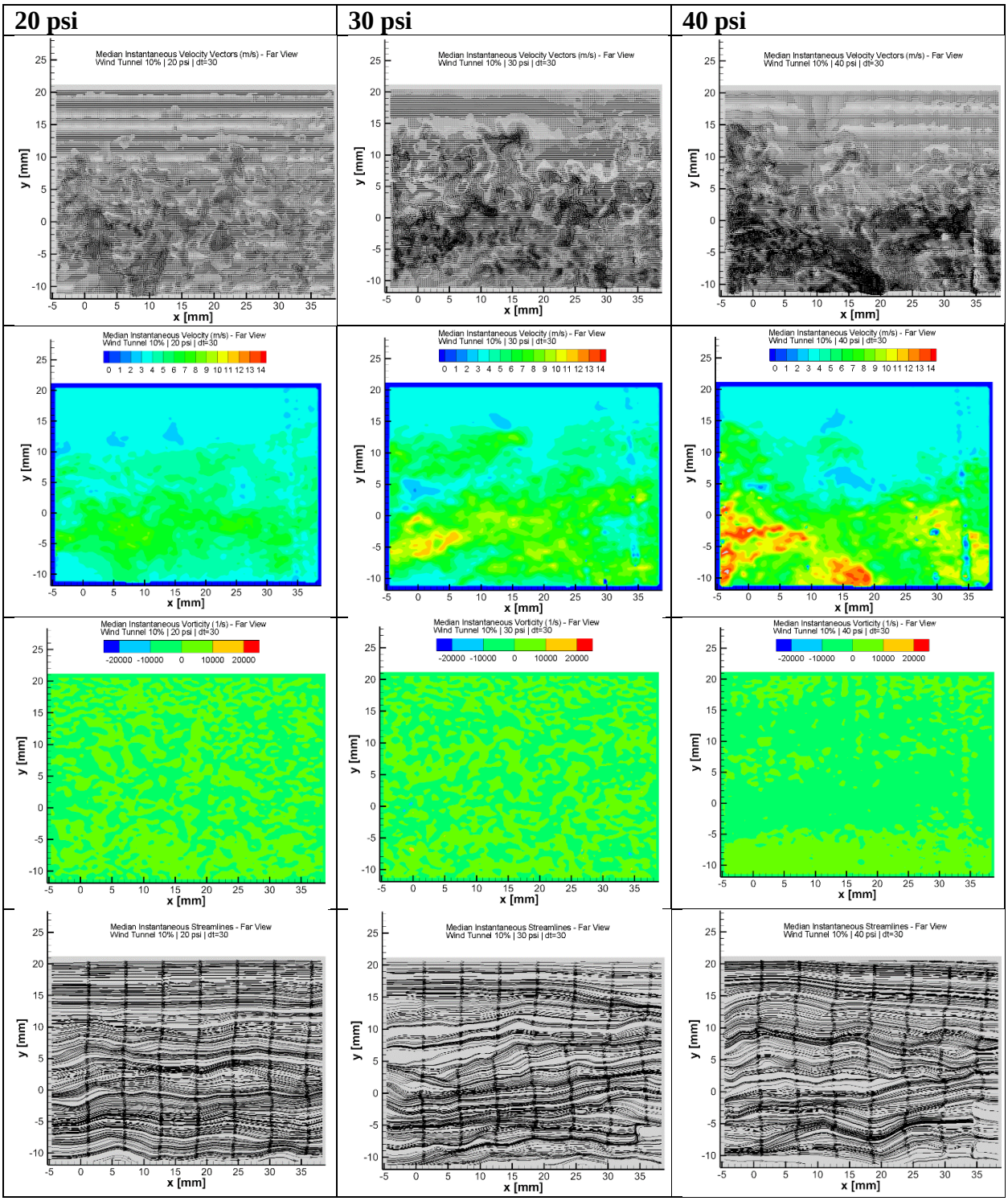

Figure B3: 2D Median Instantaneous Vortex Tube Downstream Data, 10% Wind Tunnel Speed

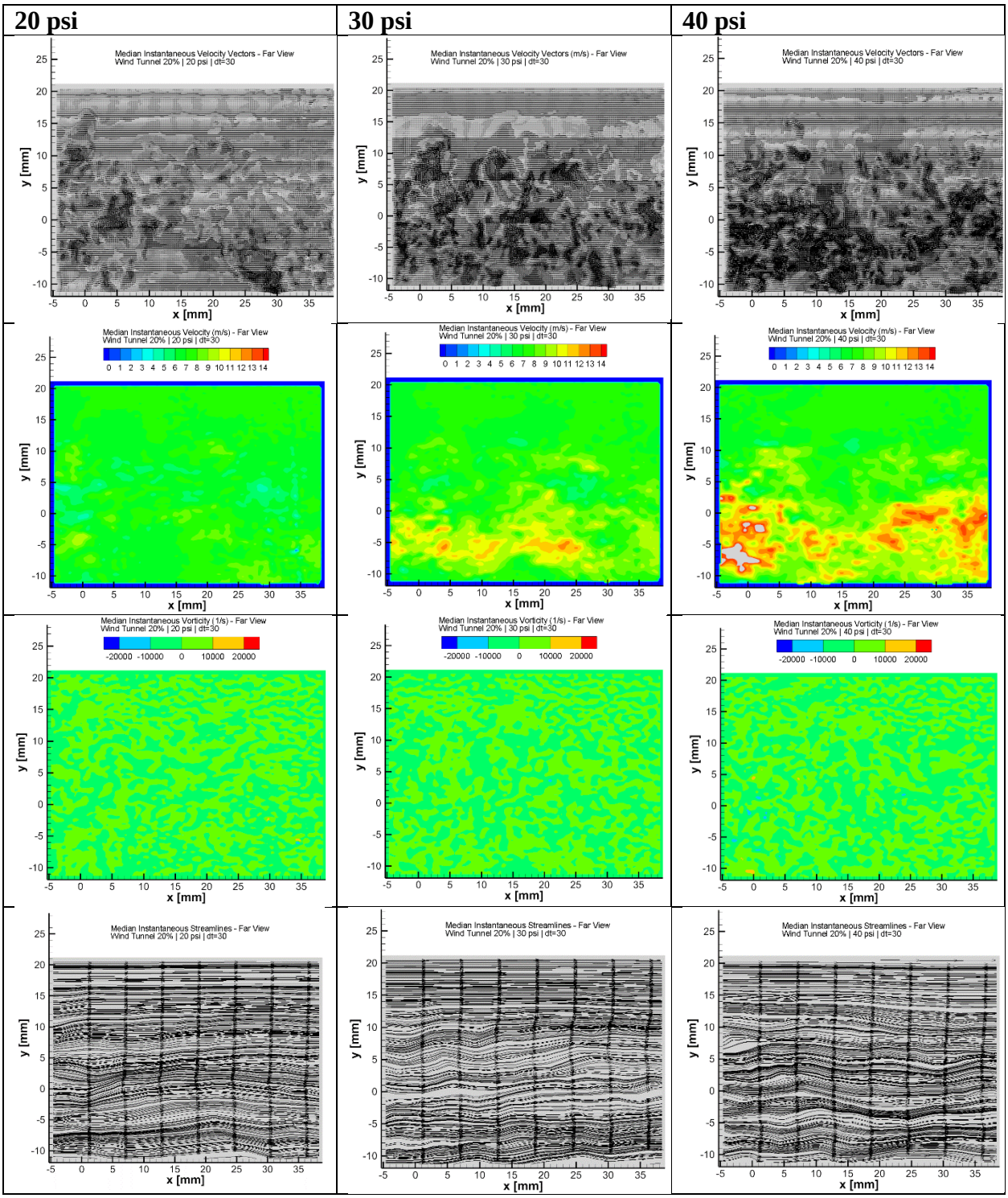

Figure B4: 2D Median Instantaneous Vortex Tube Downstream Data, 20% Wind Tunnel Speed

	20 psi	30 psi	40 psi
3%	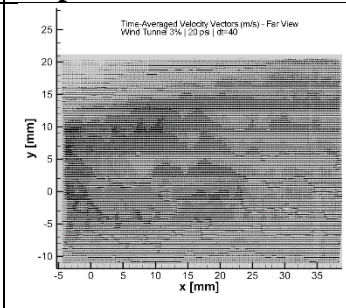	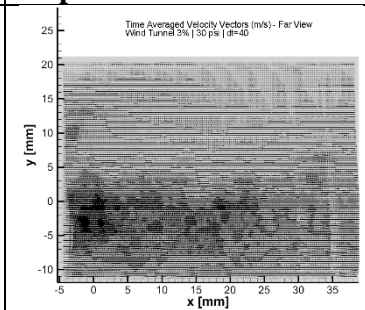	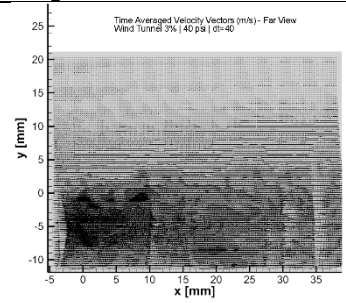
5%	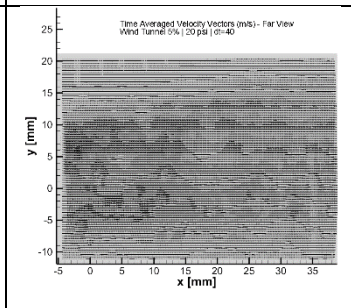	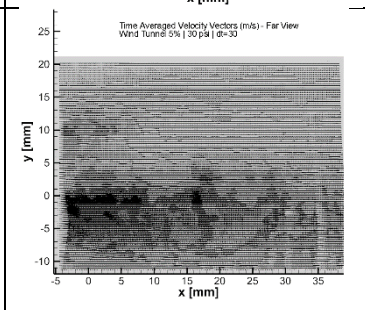	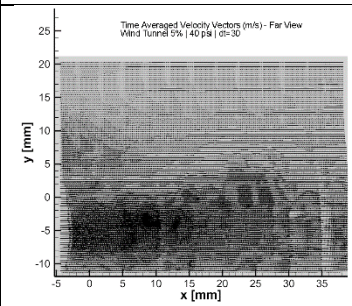
10%	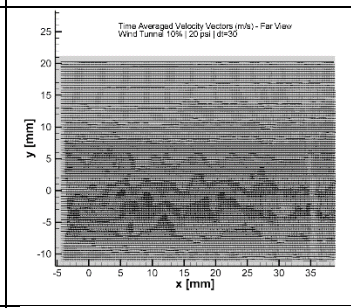	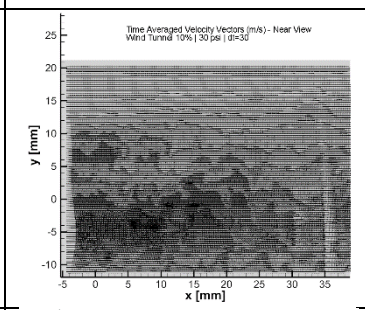	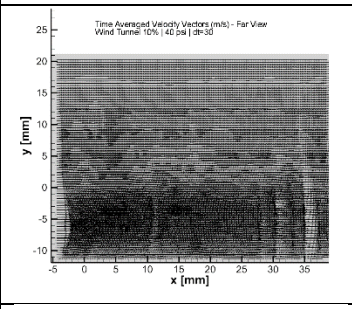
20%	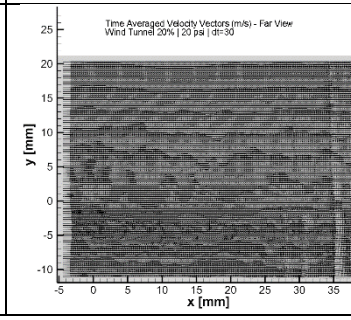	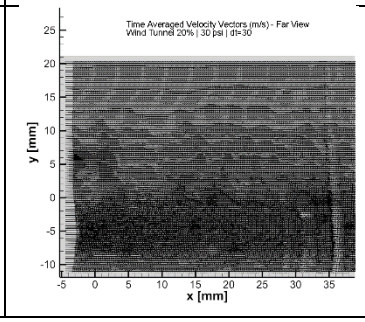	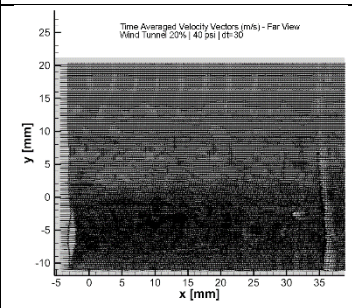

Figure B5: Time Averaged Vortex Tube Velocity Vectors from Downstream Camera

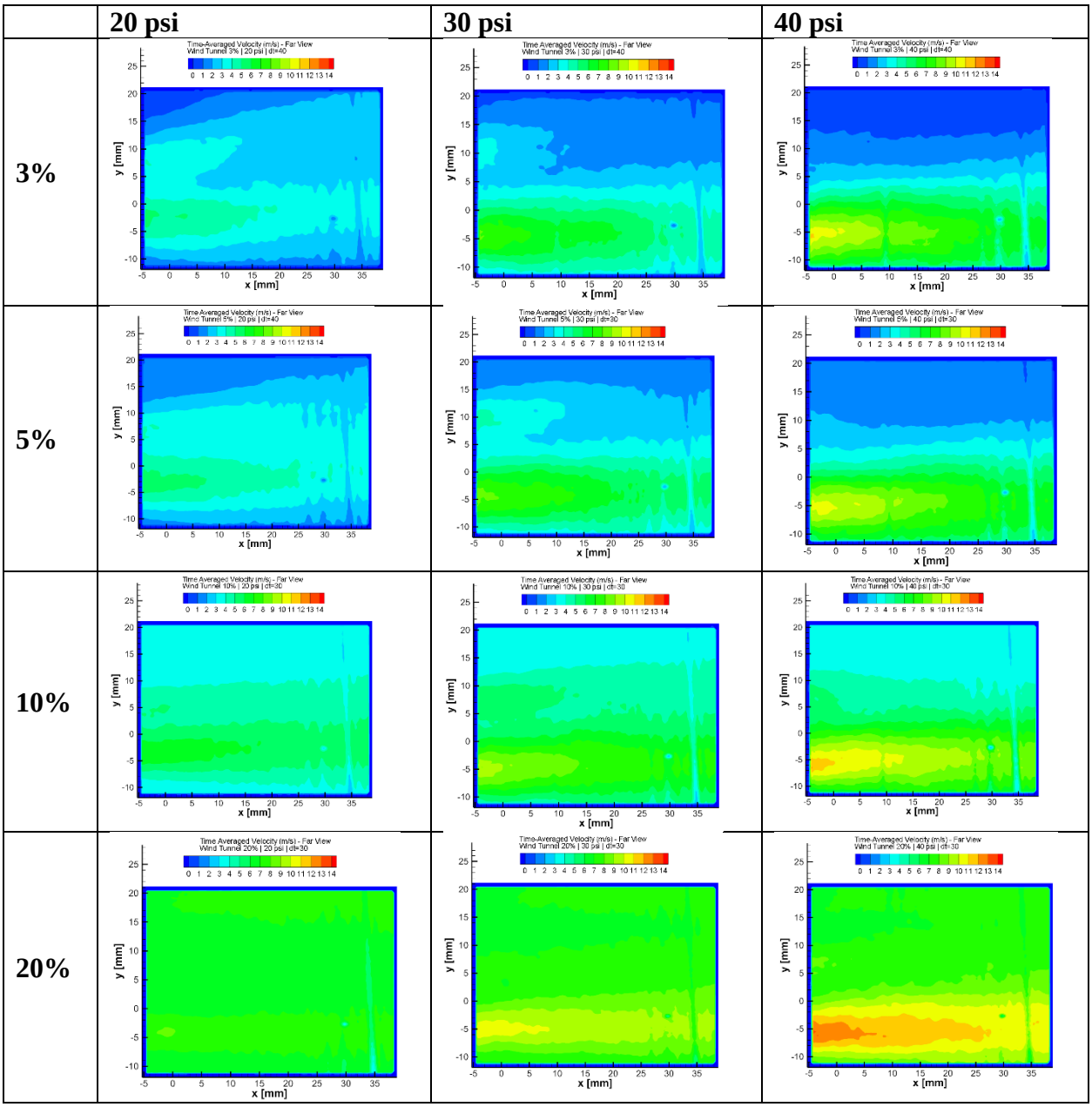

Figure B6: Time Averaged Vortex Tube Velocity Maps from Downstream Camera

APPENDIX C: 3D TOMOGRAPHIC PIV DATA

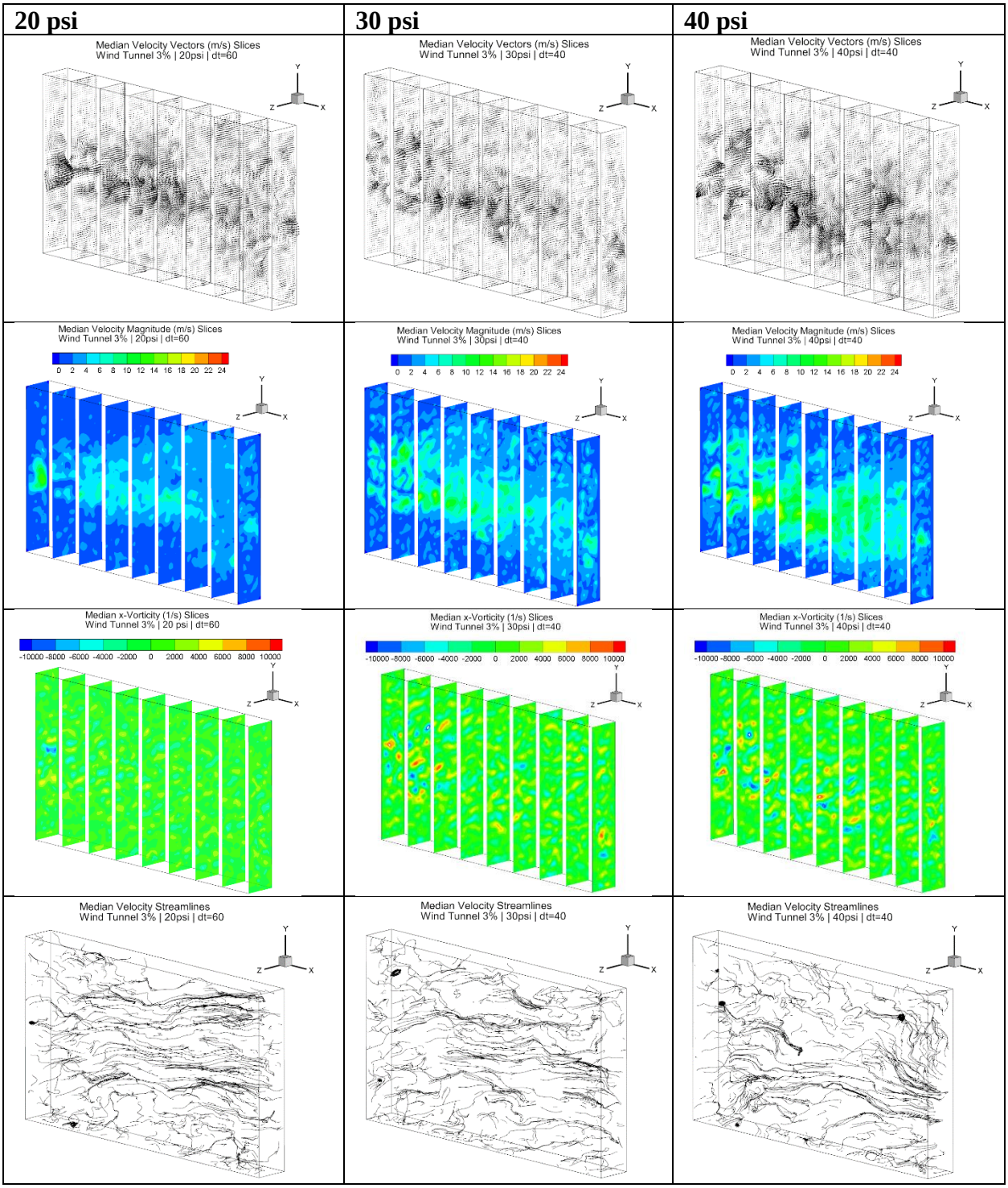

Figure C1: 3D Median Instantaneous Vortex Tube Tomographic Data, 3% Wind Tunnel Speed

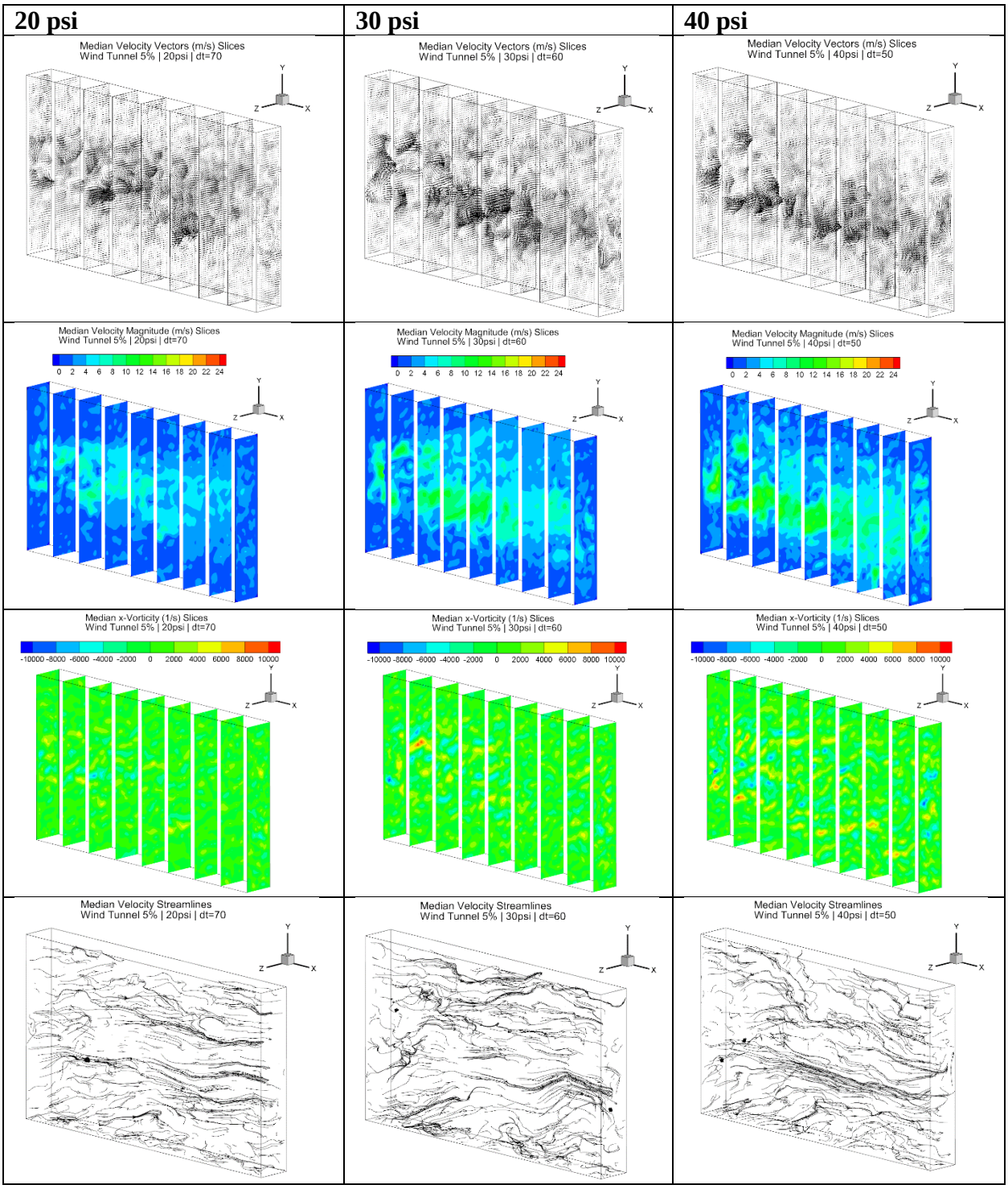

Figure C2: 3D Median Instantaneous Vortex Tube Tomographic Data, 5% Wind Tunnel Speed

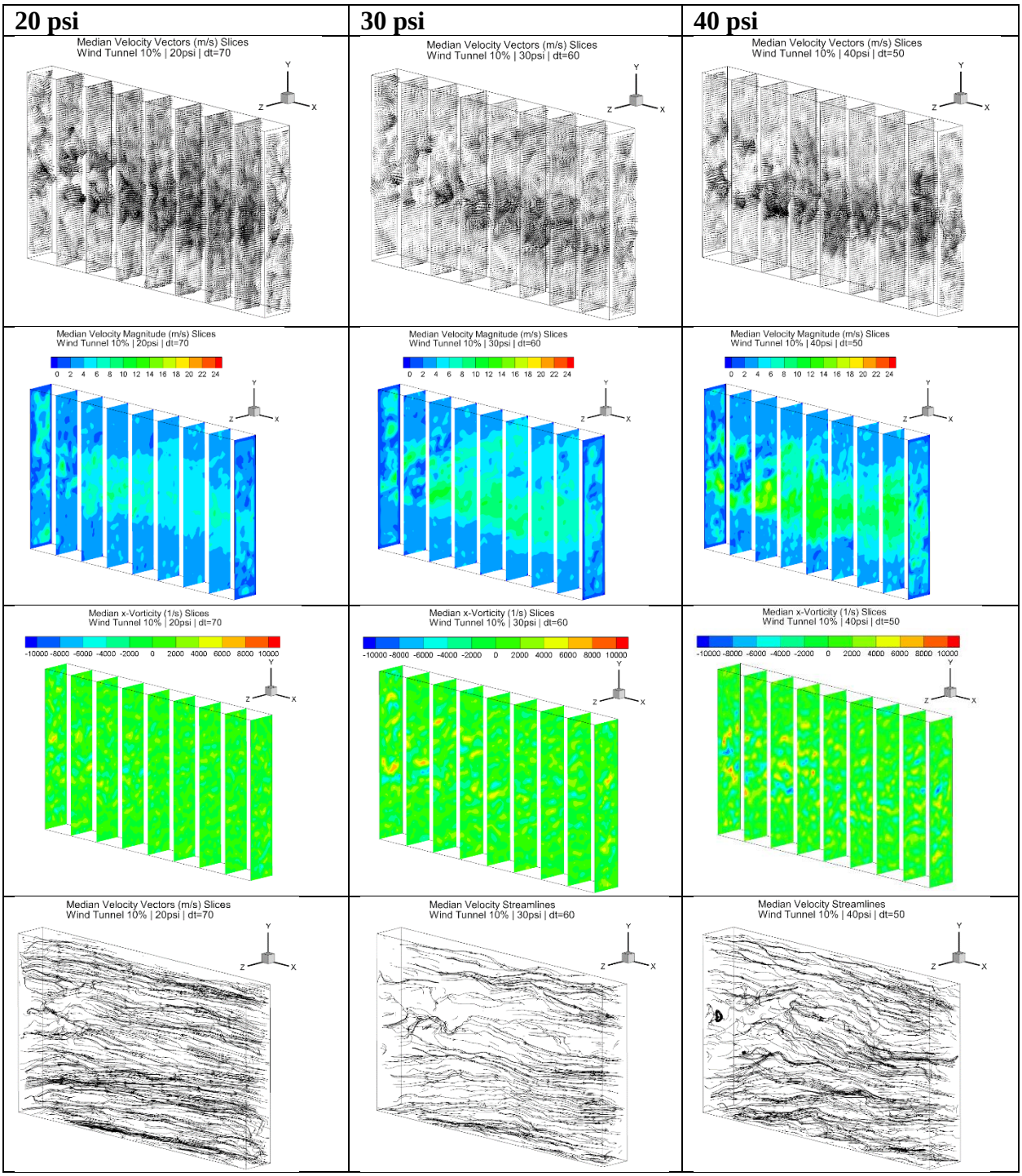

Figure C3: 3D Median Instantaneous Vortex Tube Tomographic Data, 10% Wind Tunnel Speed

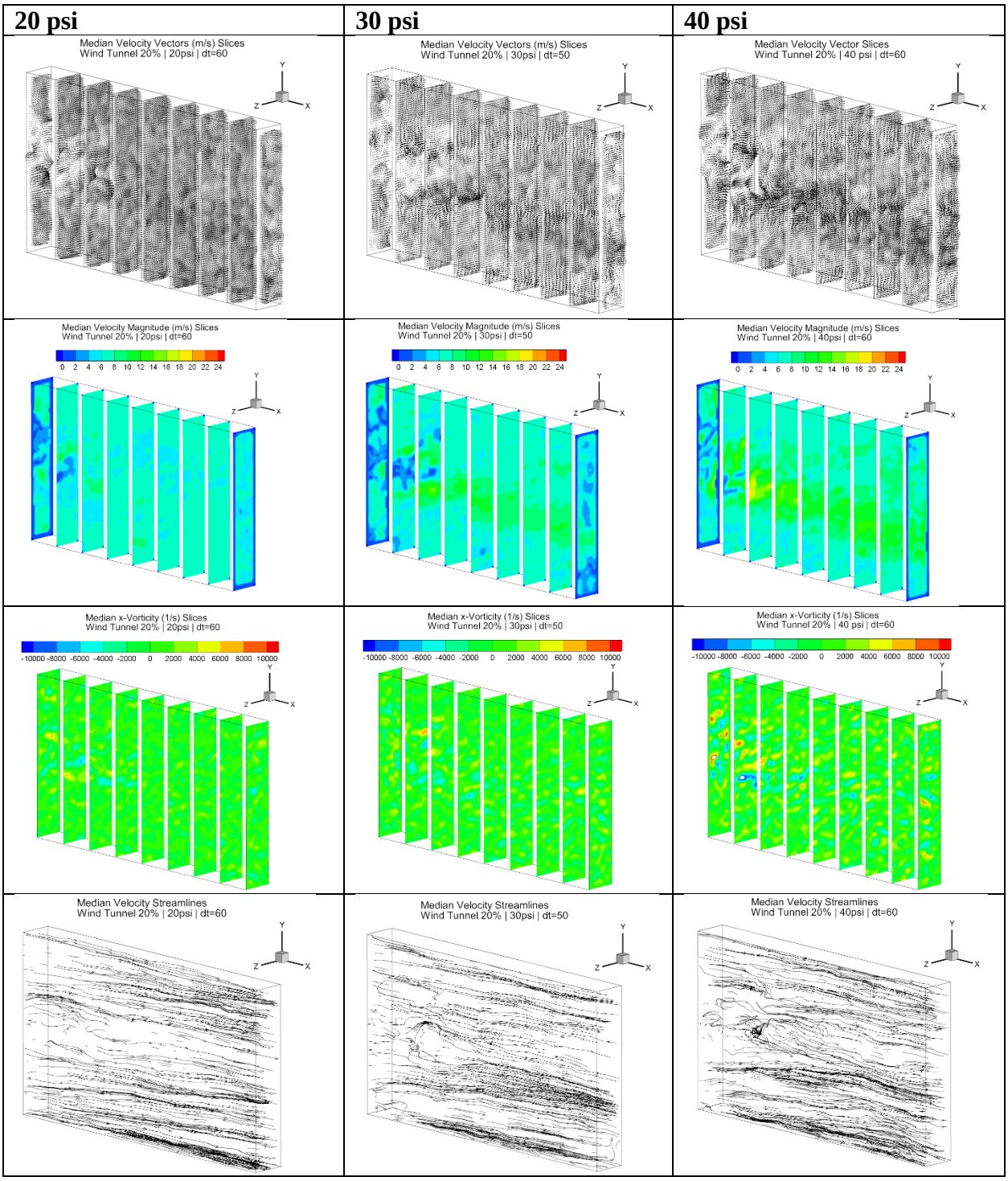

Figure C4: 3D Median Instantaneous Vortex Tube Tomographic Data, 20% Wind Tunnel Speed

	20 psi	30 psi	40 psi
3%	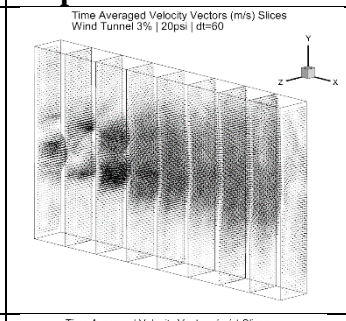	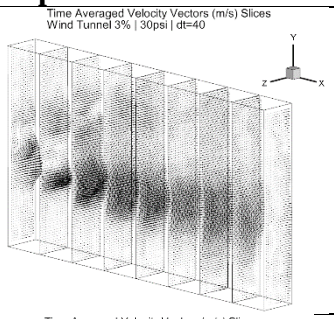	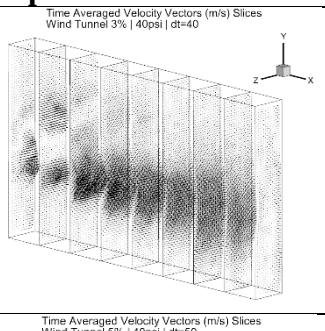
5%	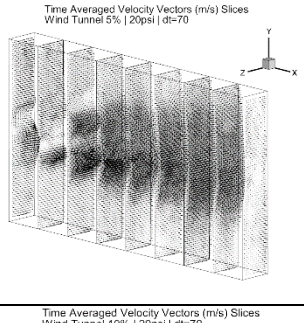	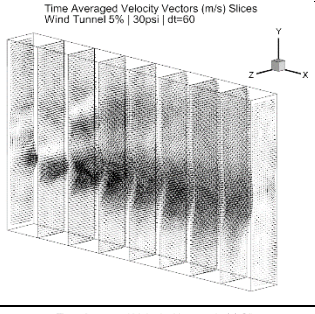	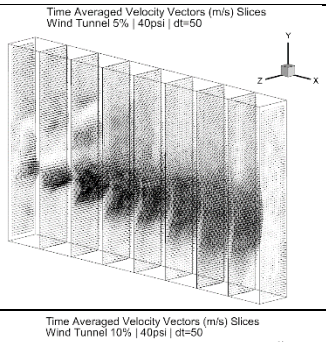
10%	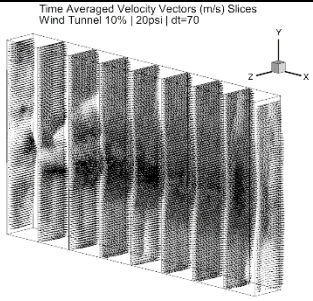	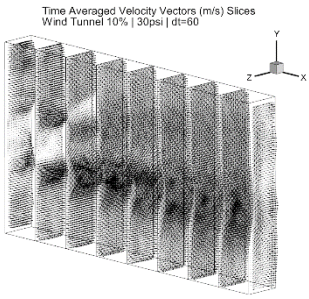	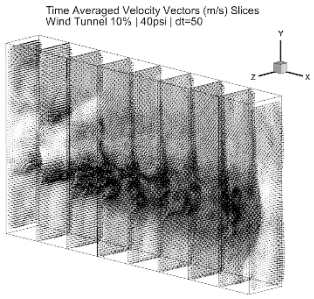
20%	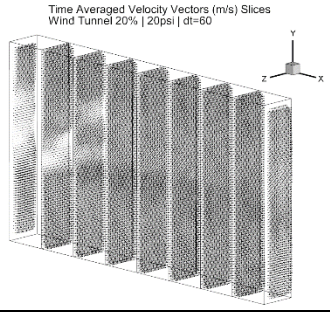	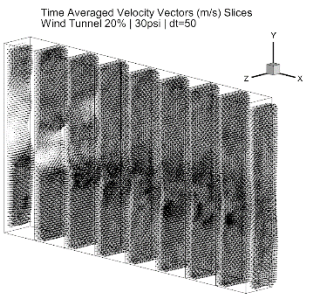	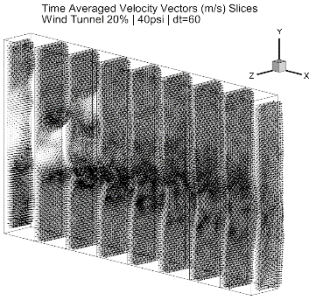

Figure C5: Time-Averaged Vortex Tube Velocity Vectors from Tomographic Data

	20 psi	30 psi	40 psi
3%	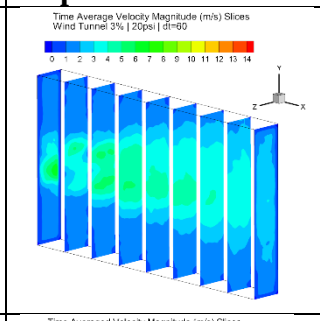	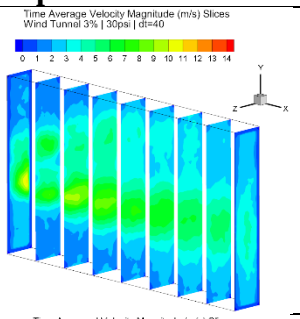	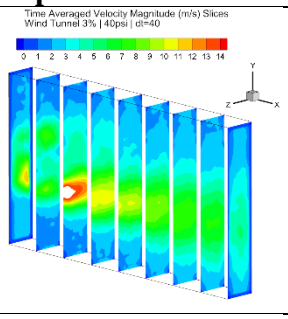
5%	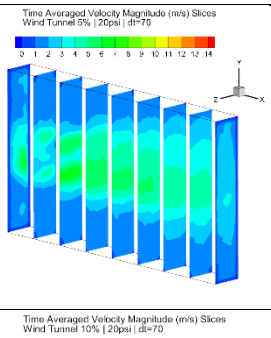	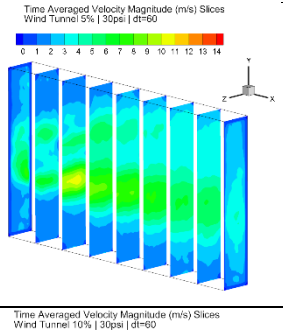	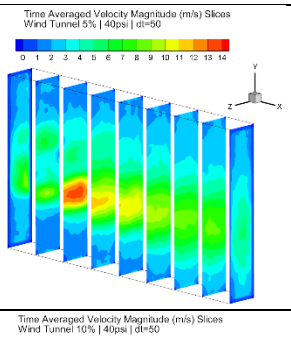
10%	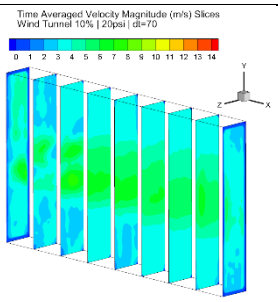	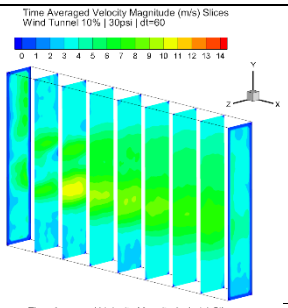	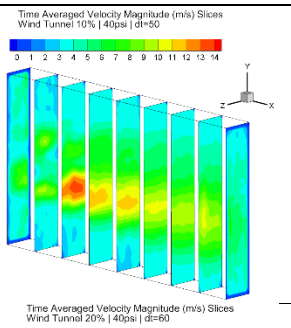
20%	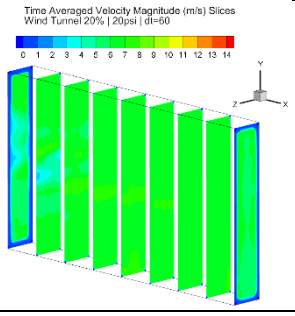	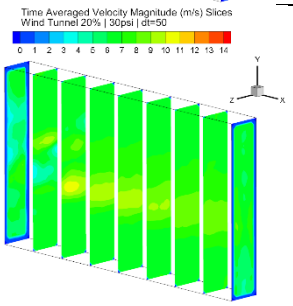	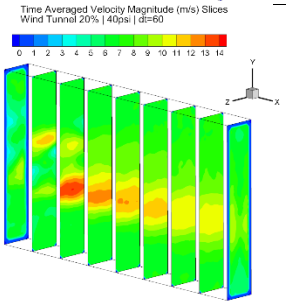

Figure C6: Time-Averaged Vortex Tube Velocity Maps from Tomographic Data

APPENDIX D: Q-CRITERION GRAPHS FROM TOMOGRAPHIC DATA

	20 psi	30 psi	40 psi
3%	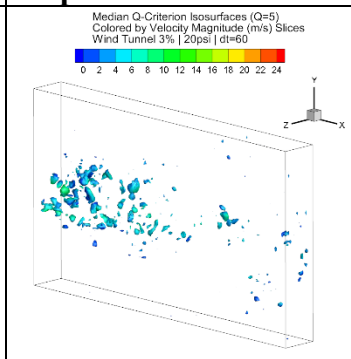	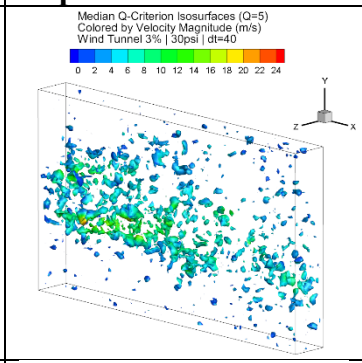	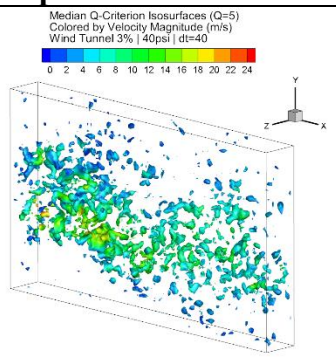
5%	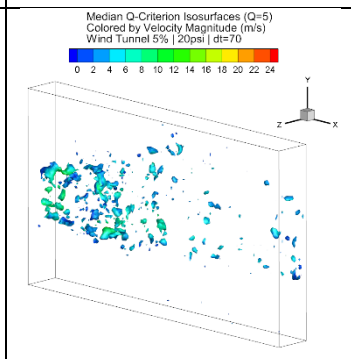	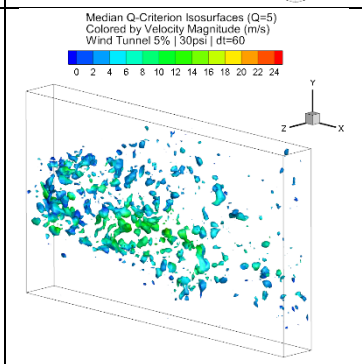	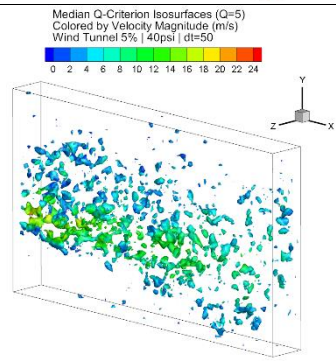
10%	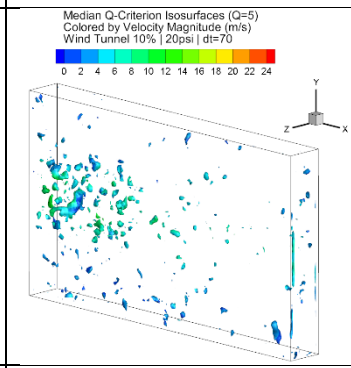	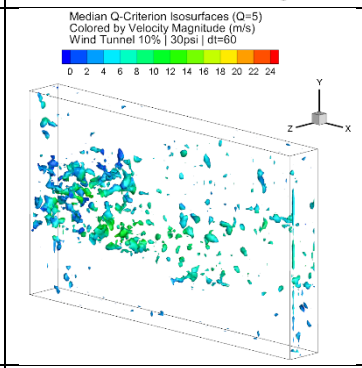	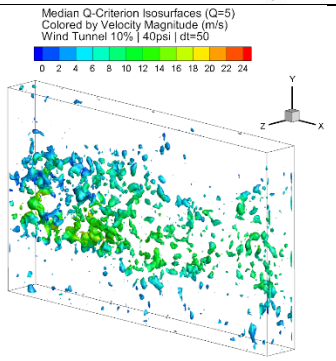
20%	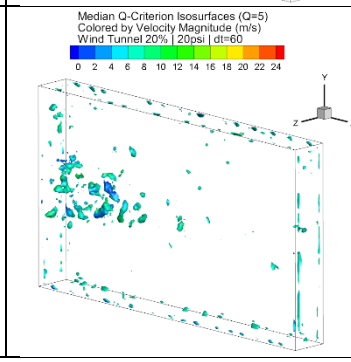	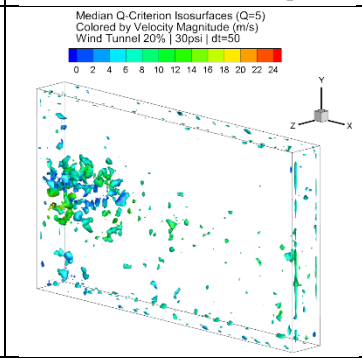	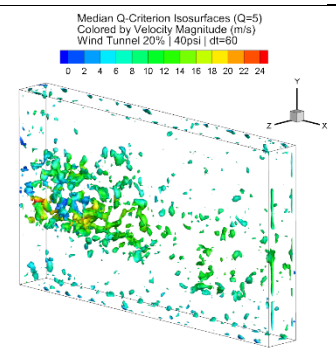

Figure D1: 3D Median Instantaneous Vortex Tube Q-Criterion Isosurfaces

APPENDIX E: AIRFOIL INTERACTION GRAPHS

	Velocity Maps	Velocity Vectors	Streamlines
Control	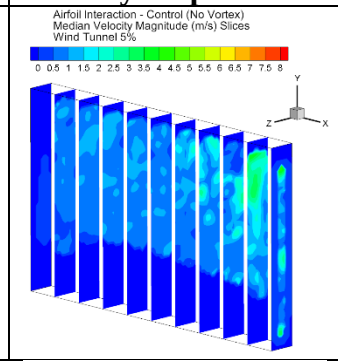	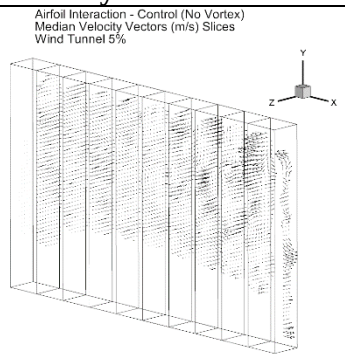	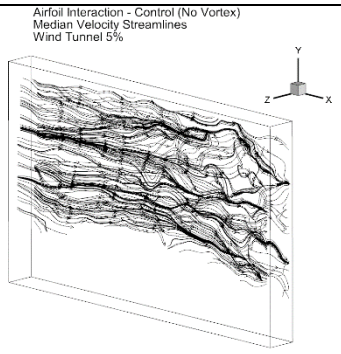
20 psi	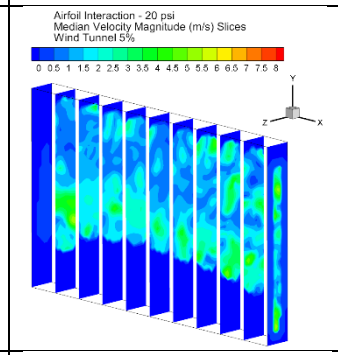	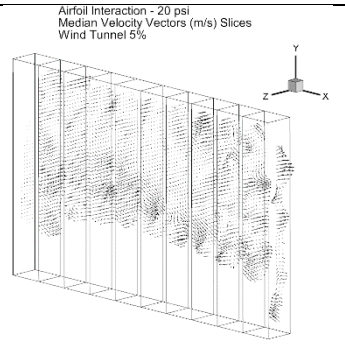	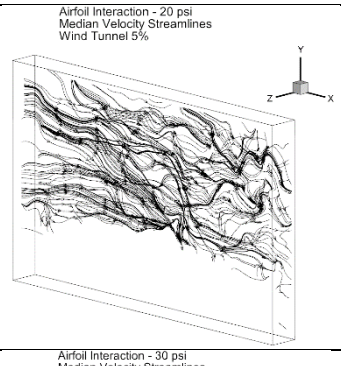
30 psi	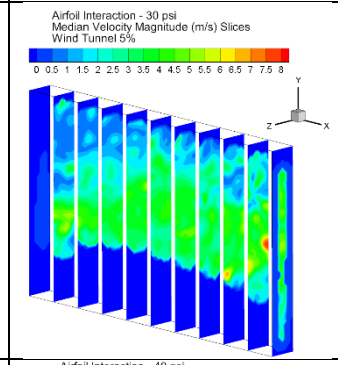	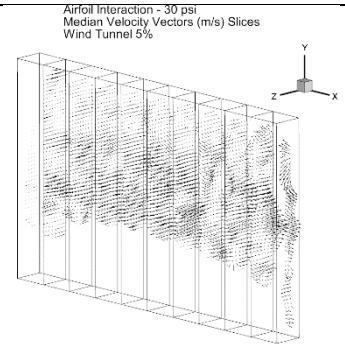	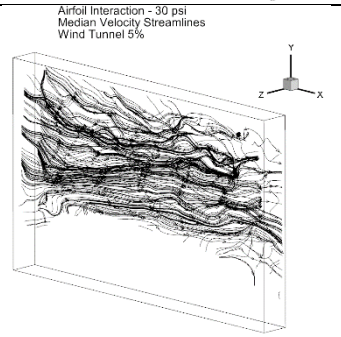
40 psi	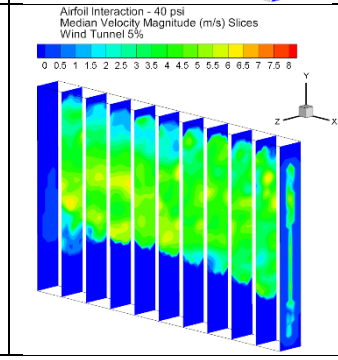	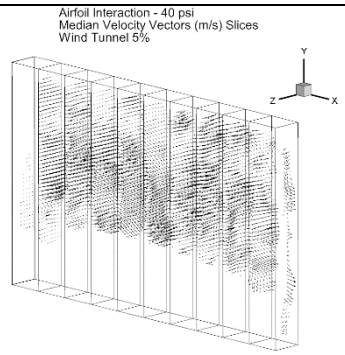	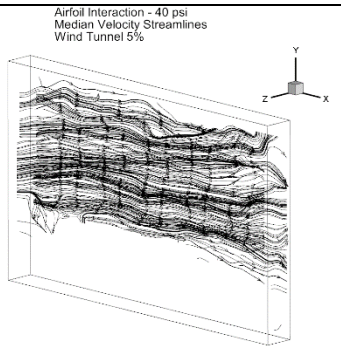

Figure E1: Airfoil Interaction 3D Median Instantaneous Velocity Maps, Vectors, Streamlines

	Average Velocity Maps	Average Velocity Vectors
Control	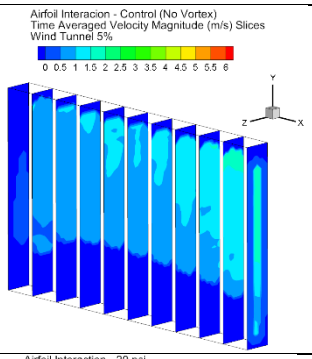	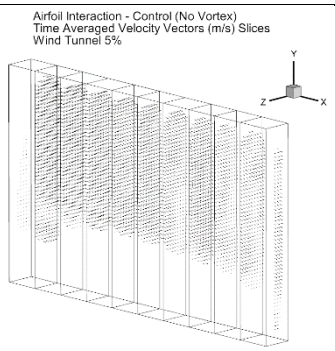
20 psi	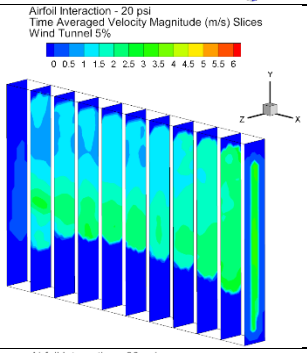	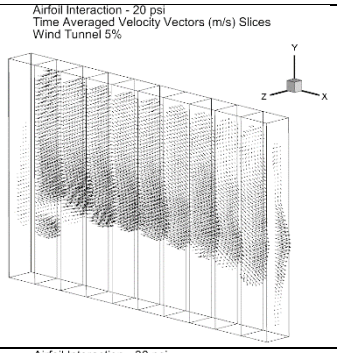
30 psi	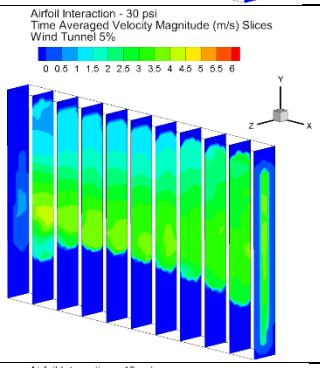	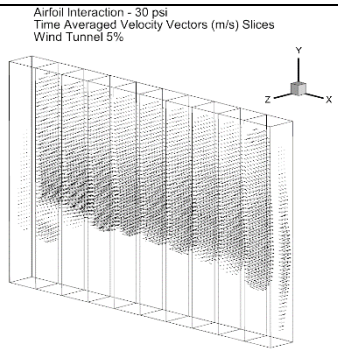
40 psi	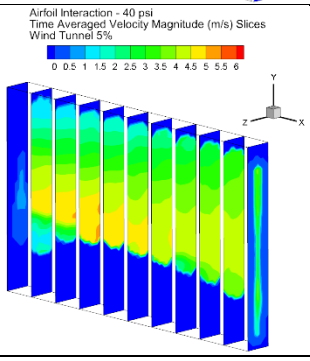	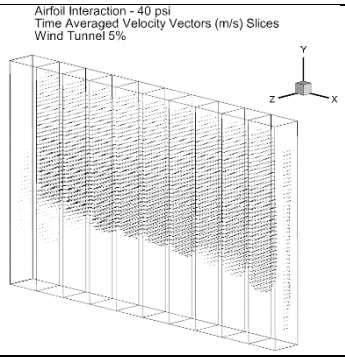

Figure E2: Airfoil Interaction 3D Time Averaged Velocity Data

	x-Vorticity Maps	Q=0 Isosurfaces	Q=0.5 Isosurfaces
Control	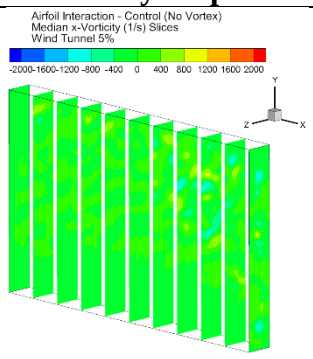	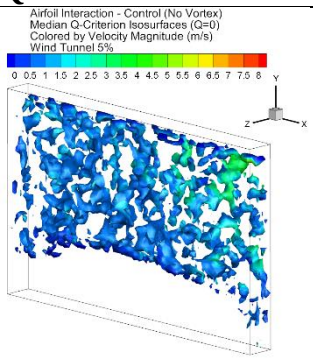	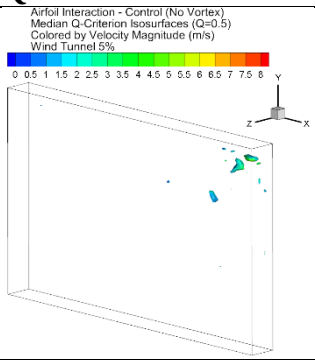
20 psi	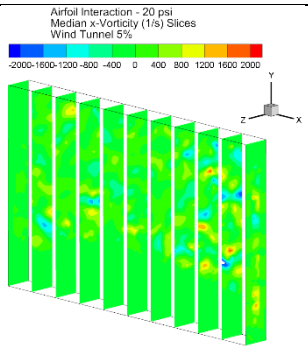	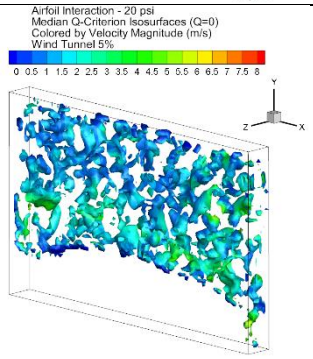	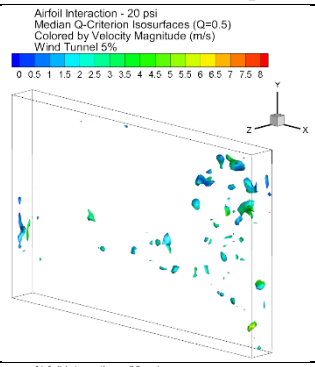
30 psi	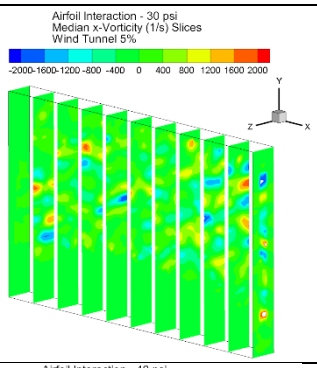	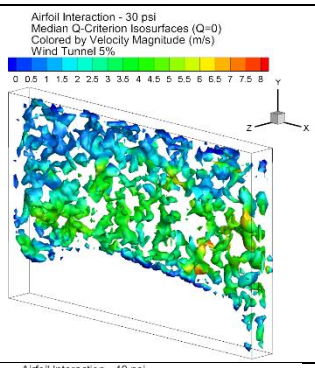	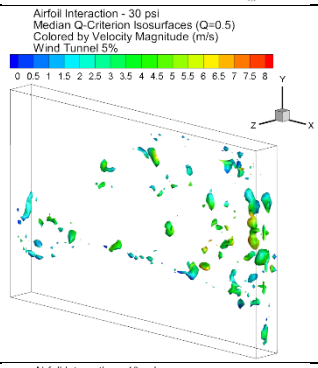
40 psi	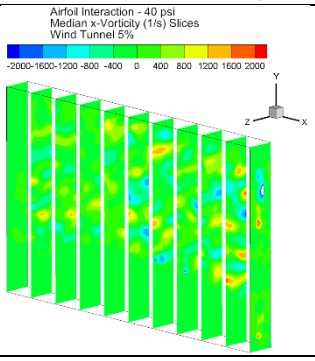	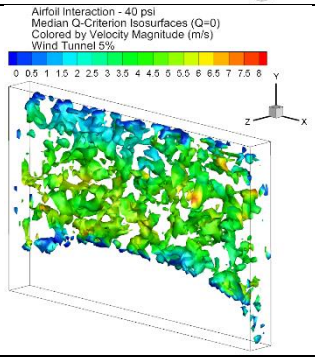	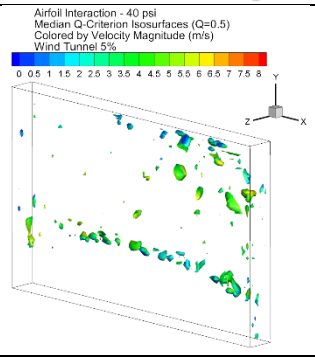

Figure E3: Airfoil Interaction 3D Median Instantaneous Vorticity Maps, Q-Criterion Isosurfaces